The Canada-France Ecliptic Plane Survey - Full Data Release: The Orbital Structure of the Kuiper Belt

Jean-Marc C. Petit, J.J. Kavelaars, B.J. Gladman, R.L. Jones, J.Wm. Parker, C. van Laerhoven, P. Nicholson, G. Mars, P. Rousselot, O. Mousis, et al.

to appear in the Astronomical Journal (submitted 25 May 2011)

The Canada-France Ecliptic Plane Survey - Full Data Release: The orbital structure of the Kuiper belt[1]

J-M. Petit[2,4], J.J. Kavelaars[3], B.J. Gladman[4], R.L. Jones[3,4], J.Wm. Parker[5], C. Van Laerhoven[4,6], P. Nicholson[7], G. Mars[8], P. Rousselot[2], O. Mousis[2], B. Marsden[9,12] A. Bieryla[5], M. Taylor[10], M.L.N. Ashby[9], P. Benavidez[11], A. Campo Bagatin[11], G. Bernabeu[11]

ABSTRACT

We report the orbital distribution of the trans-neptunian objects (TNOs) discovered during the Canada-France Ecliptic Plane Survey (CFEPS), whose discovery phase ran from early 2003 until early 2007. The follow-up observations started just after the first discoveries and extended until late 2009. We obtained characterized observations of 321 sq.deg. of sky to depths in the range g $\sim$23.5 - 24.4 AB mag. We provide a database of 169 TNOs with high-precision dynamical classification and known discovery efficiency. Using this database, we find that the classical belt is a complex region with sub-structures that go beyond the usual splitting of inner (interior to 3:2 mean-motion resonance [MMR]), main (between 3:2 and 2:1 MMR), and outer (exterior to 2:1 MMR). The main classical belt (a=40–47 AU) needs to be modeled with

[1]Based on observations obtained with MegaPrime/MegaCam, a joint project of CFHT and CEA/DAPNIA, at the Canada-France-Hawaii Telescope (CFHT) which is operated by the National Research Council (NRC) of Canada, the Institute National des Sciences de l'Universe of the Centre National de la Recherche Scientifique (CNRS) of France, and the University of Hawaii. This work is based in part on data products produced at the Canadian Astronomy Data Centre as part of the Canada-France-Hawaii Telescope Legacy Survey, a collaborative project of NRC and CNRS.

[2]Institut UTINAM, CNRS-UMR 6213, Observatoire de Besançon, BP 1615, 25010 Besançon Cedex, France

[3]Herzberg Institute of Astrophysics, National Research Council of Canada, Victoria, BC V9E 2E7, Canada

[4]Department of Physics and Astronomy, 6224 Agricultural Road, University of British Columbia, Vancouver, BC, Canada

[5]Planetary Science Directorate, Southwest Research Institute, 1050 Walnut Street, Suite 300, Boulder, CO 80302, USA

[6]Department of Planetary Sciences, University of Arizona, 1629 E. University Blvd, Tucson, AZ, 85721-0092, USA

[7]Cornell University, Space Sciences Building, Ithaca, New York 14853, USA

[8]Observatoire de la Cote d'Azur, BP 4229, Boulevard de l'Observatoire, F-06304 Nice Cedex 4, France

[9]Harvard-Smithsonian Center for Astrophysics, 60 Garden Street, Cambridge, MA 02138

[10]Department of Physics and Astronomy, University of Victoria, Victoria, BC V8W 2Y2, Canada

[11]Departamento de Fisica, Ingenieria de Sistemas y Teoria de la Señal, E.P.S.A., Universidad de Alicante, Apartado de Correos 99, Alicante 03080, Spain

[12]Deceased

at least three components: the 'hot' component with a wide inclination distribution and two 'cold' components (stirred and kernel) with much narrower inclination distributions. The hot component must have a significantly shallower absolute magnitude (H_g) distribution than the other two components. With 95% confidence, there are 8000^{+1800}_{-1600} objects in the main belt with $H_g \leq 8.0$, of which 50% are from the hot component, 40% from the stirred component and 10% from the kernel; the hot component's fraction drops rapidly with increasing H_g. Because of this, the apparent population fractions depend on the depth and ecliptic latitude of a trans-neptunian survey. The stirred and kernel components are limited to only a portion of the main belt, while we find that the hot component is consistent with a smooth extension throughout the inner, main and outer regions of the classical belt; in fact, the inner and outer belts are consistent with containing only hot-component objects. The $H_g \leq 8.0$ TNO population estimates are 400 for the inner belt and 10,000 for the outer belt to within a factor of two (95% confidence). We show how the CFEPS Survey Simulator can be used to compare a cosmogonic model for the the orbital element distribution to the real Kuiper belt.

Subject headings: Kuiper Belt, surveys; PACS 96.30.Xa

1. Introduction

The minor body populations of the solar system provide, via their orbital and physical properties, windows into the dynamical and chemical history of the Solar System. Recognition of the structural complexity in the trans-neptunian region has lead to models that describe possible dynamical evolutionary paths, such as a smooth migration phase for Neptune (Malhotra 1993), the large scale re-ordering of the outer solar system (Tsiganis et al. 2005; Thommes et al. 1999), the scattering of now-gone rogue planets (Gladman & Chan 2006), or the close passage of a star (Ida et al. 2000). Evaluating these models is fraught with dangers due to observational biases affecting our knowledge of the intrinsic populations of the trans-neptunian region (see Kavelaars et al. 2008; Jones et al. 2010, for discussion of these issues). Over the past twenty years, many different Kuiper Belt surveys (those with more than 10 detections include Jewitt et al. (1996); Larsen et al. (2001); Trujillo et al. (2001); Gladman et al. (2001); Allen et al. (2002); Millis et al. (2002); Elliot et al. (2005); Petit et al. (2006); Jones et al. (2006); Schwamb et al. (2010)) have been slowly building up a sample, albeit with differing flux and pointing biases. Jones et al. (2006) enumerates the aspects of surveys that must be carefully recorded and made public if quantitative comparisons with models are to be made.

The primary goal of the Canada-France Ecliptic Plane Survey (CFEPS) is the production of a catalogue of trans-neptunian objects (TNOs) combined with a precise account of the observational biases inherent to that catalog. The description of the biases, combined with provisioning of a 'survey simulator', enables researchers to quantitatively compare the outcome of their model simulations to the observed TNO populations. In Jones et al. (2006) we described our initial 'pre-survey' and general motivation for this project, and Kavelaars et al. (2009) (P1 hereafter) describes the first year of operation of this survey (the L3 data release). This manuscript describes the observations that make up the integrated seven years of the project and provide our complete catalog (the L7 release) of near-ecliptic detections and characterizations along with fully-linked high-quality orbits. In summary, the 'products' of the CFEPS survey consists of four items:

1. A list of detected CFEPS TNOs, associated with the block of discovery,
2. a characterization of each survey block,
3. a Survey Simulator that takes the a proposed Kuiper Belt model, exposes it to the known detection biases of the CFEPS blocks and produces simulated detections to be compared with the real detections, and
4. the CFEPS-L7 model population.

In Sections 2 and 3, we describe the observation and characterization of the CFEPS TNO sample. The dynamical classification of all tracked TNOs in our sample is given in Section 4. In Section 5, we update our parametrized model of the main and inner classical Kuiper Belt (P1) and give an improved estimate of the total number of objects in each of these dynamical subpopulations. We also extend our model to the non-resonant, non-scattering part of the belt beyond the 2:1 MMR with Neptune. Section 6 gives an order of magntitude estimate of the scattering disk's population. Section 7 demonstrates the use of our Survey

Simulator to compare the results of a cosmogonic model to the CFEPS detections. Finally in Section 8, we present our conclusions and put our findings in perspective.

2. Observations and Initial reductions

The discovery component of the CFEPS project imaged ∼320 square degrees of sky, almost all of which was within a few degrees of the ecliptic plane. Discovery observations occurred in blocks of ≈ 16 fields acquired using the Canada-France-Hawaii Telescope (CFHT) MegaPrime camera which delivered discovery image quality (FWHM) of 0.7 - 0.9 arc-seconds in queue-mode operations. The $0.96^\circ \times 0.94^\circ$ MegaPrime FOV is paved by 36 individual 4600x2048 CCDs, each pixel having a scale of $0.187''$.

The CFEPS designation of a 'block' of discovery fields was: a leading 'L' followed by the year of observations (3,4,5 and 7) and then a letter representing the two week period of the year in which the discovery observations were acquired (example: L3f occured in the second half of March 2003). Discovery observations occurred between March 2003 and July 2005 plus one block of fields (L7a) observed in January 2007. The CFEPS presurvey block (Jones et al. 2006) in 2002 also consisted of a single contiguous sky patch. To enhance our sensitivity to the latitude distribution of the Kuiper belt we also acquired two survey blocks of 11 square degrees each, at ∼10° ecliptic latitude (L5r) and ∼20° ecliptic latitude (L5s). Each of the discovery blocks was searched for TNOs using our Moving Object Pipeline (MOP; see Petit et al. 2004). Table 1 provides a summary of the survey fields, imaging circumstances and detection thresholds, both for CFEPS and for the presurvey. Figure 1 presents the sky coverage of our discovery blocks. For a detailed description of the initial CFEPS observing plan, field sequencing and follow-up strategy see Jones et al. (2006) and P1.

3. Sample Characterization

The photometric calibration of the discovery triplets to a common reference frame and determination of our detection efficiency is required for our survey simulator analysis. It is presented in Appendix B and the photometric measurements of all CFEPS TNOs acquired in photometric conditions are given in Table 7.

We characterized the magnitude-dependent detection probability of each discovery block by inserting artificial sources in the images and running these images through our detection pipeline to recover these artificial sources. We used the g filter at CFHT for all our discovery observations, except for block L3h which was acquired using the r filter. For that block's fields, we shifted the limits to a nominal g value using a color of $(g - r) = 0.70$, corresponding to the mean $(g - r)$ color of our full CFEPS sample. The TNOs in each block that have a magnitude brighter than that block's 40% detection probability are considered to be part of the CFEPS *characterized sample*. Because detection efficiencies below $\sim 40\%$ determined by human operators and our MOP diverge - MOP accepts more faint objects, at the expense of false detections - (Petit et al. 2004), and since characterization is critical to the CFEPS goals, we chose not to utilize the sample faint-ward of the measured 40% detection-efficiency level for quantitative science (although we report these

Table 1. Summary of Field positions and Detections.

Block	RA[a]	DEC[a]	Fill[b]	Charact. Det.[c]		Geometry	Discovery		limit[d]	Detection limits[e]	
	HRS	DEG	Factor	Disc.	Track.	DEG x DEG	date	filter	g_{AB}	rate (“/h)	direction (DEG)
L3f	12:42	−04:33	0.80	3	2	4x4	2003-03-24	G.MP9401	23.75	1.7 to 5.1	−10.0 to 50.0
L3h	13:03	−06:48	0.81	14	11	4x4	2003-04-26	R.MP9601	24.43†	0.8 to 6.2	5.6 to 41.6
L3q	22:01	−12:04	0.89	9	7	4x4	2003-08-31	G.MP9401	24.08	1.2 to 6.2	−38.0 to −2.0
L3s	19:43	−01:20	0.87	5	5	14x1	2003-09-23	G.MP9401	23.95	0.8 to 8.0	−42.6 to −5.0
L3w	04:33	22:21	0.87	13	11	16x1	2003-12-16	G.MP9401	24.25	0.8 to 6.0	−29.0 to 11.0
L3y	07:30	21:48	0.85	10	10	4x4	2003-12-24	G.MP9401	24.08	1.7 to 5.1	−6.0 to 24.0
		Total		54	46	94 sqr. deg.					
L4h	13:35	−09:00	0.89	20	16	7x2; 1x1	2004-04-26	G.MP9401	24.06	0.8 to 6.0	2.0 to 42.0
L4j	15:12	−16:51	0.89	10	10	8x2	2004-04-25	G.MP9401	24.00	0.8 to 5.6	−3.6 to 36.4
L4k	15:12	−18:47	0.90	19	16	8x2	2004-05-24	G.MP9401	24.35	0.8 to 5.7	−1.0 to 35.0
L4m	19:14	−22:47	0.89	4	4	12x1	2004-06-25	G.MP9401	23.76	0.8 to 5.6	−25.0 to 15.0
L4n	19:23	−21:33	0.90	4	4	14x1	2004-07-22	G.MP9401	23.74	0.8 to 6.0	−27.7 to 12.3
L4o	19:15	−23:46	0.90	2	1	13x1	2004-07-24	G.MP9401	23.53	0.8 to 6.0	−24.7 to 11.3
L4p	20:53	−18:27	0.85	9	9	8x2	2004-08-15	G.MP9401	24.00	1.0 to 5.7	−30.0 to 0.0
L4q	21:26	−16:05	0.85	14	10	8x2	2004-08-19	G.MP9401	24.21	1.2 to 6.1	−35.5 to −0.5
L4v	02:35	15:10	0.78	18	14	2x2; 1x1; 5x2	2004-11-09	G.MP9401	24.40	0.8 to 6.3	−34.0 to −2.0
		Total		100	84	133 sqr. deg.					
L5c	09:11	17:13	0.84	21	19	7x2; 1x1	2005-02-10	G.MP9401	24.30	0.8 to 6.4	−1.0 to 31.0
L5i	16:18	−22:18	0.90	7	7	8x2	2005-05-12	G.MP9401	23.84	0.4 to 7.3	−9.4 to 32.2
L5j	16:09	−19:59	0.89	3	3	8x2	2005-06-10	G.MP9401	23.49	0.4 to 7.0	−9.9 to 33.9
L5r	22:36	03:55	0.90	1	1	3x2; 1x1; 2x2	2005-09-03	G.MP9401	23.89	0.7 to 7.5	−42.1 to −1.9
L5s	22:28	14:35	0.90	1	1	3x2; 1x1; 2x2	2005-09-03	G.MP9401	24.00	0.7 to 7.5	−41.8 to −2.0
L7a	08:43	18:30	0.89	9	8	patchy	2007-01-19	G.MP9401	23.98	0.8 to 7.7	−4.1 to 34.9
		Total		42	39	94 sqr. deg.					
		Grand Total		196	169	321 sqr. deg.					
Pre	22:00	-13:00	0.90	13	10	3.5x2	2002-08-05	R	24.85⋆	0.8 to 8.0	−35.0 to −5.0

Note. — (a) RA/DEC is the approximate center of the field. (b) Fill Factor is the fraction of the rectangle covered by the mosaic and useful for TNO searching. (c) The number of objects in columns 5 and 6 correspond to those detected and tracked in the characterized sample, as defined in Sect. 3. (d) The limiting magnitude of the survey, g_{AB}, is in the SDSS photometric system and corresponding to a 40% efficiency of detection. (e)Detection limits give the limits on the sky motion in rate (“/hr) and direction (“zero degrees” is due West, and positive to the North). † Although the L3h block was acquired in r filter, the reported limiting magnitude has been translated to g band by applying an offset of $g - r = 0.7$, which is the average $g - r$ color of our full sample (see Table 7). ⋆ The Presurvey block was acquired in R filter with the CFH12K camera (Jones et al. 2006). The limiting magnitude has been translated to g band by applying an offset of $g - R = 0.8$.

discoveries, many of which were tracked to precise orbits). The *characterized* CFEPS sample consists of 196 objects of the 231 discovered (see Table 7 for a list of these TNOs). The fraction of objects detected bright-ward of our cutoff is consistent with the shape of the TNO luminosity function (Petit et al. 2008) and typical decay in detection efficiency due to gradually increasing stellar confusion and the rapid fall-off at the SNR limit.

Our discovery and tracking observations were made using short exposures designed to maximize the efficiency of detection and tracking of the TNOs in the field. These observations do not provide the high-precision flux measurements necessary for possible classification based on broadband colors of TNOs and we do not comment here on this aspect of the CFEPS sample.

4. Tracking and Lost Objects

Tracking during the first opposition was done using the built-in followup of the CFEPS project. Subsequent tracking, over the next 3 oppositions, occurred at a variety of facilities, including CFHT. The observational efforts outside CFHT are summarized in Table 2. In spring 2006 the CFEPS project made an initial data release of the complete observing record for the L3 objects (objects discovered in 2003; before all the refinement observations for all objects were complete). The L3 release was reported to the Minor Planet Center (MPC) (Gladman et al. 2006; Kavelaars et al. 2006a,b) and additional followup that has occurred since the 2006 release has also been reported to the MPC. The final release of the complete observing record for all remaining CFEPS objects is available from the MPC (Kavelaars et al. 2011). Detailed astrometric and photometric data for the CFEPS objects can be found on the CFEPS specific databases[1]. The correspondence between CFEPS internal designations and MPC designations can be determined using Tables 3 and 4, or from electronic tables on the *cfeps.net* site. All characterized and tracked objects are prefixed by *L* and are used with the survey simulator for our modeling below. The tracking observations provide sufficient information to allow reliable orbits to be determined such that unambiguous dynamical classification can be achieved in nearly all cases. Ephemeris errors are smaller than a few tens of arc-seconds over the next 5 years. Our standard was to pursue tracking observations until the semimajor axis uncertainty was $< 0.1\%$; in Tables 3 and 4, orbital elements are shown to the precision with which they are known, with typical fractional accuracies on the order of 10^{-4} or better. In the cases of resonant objects even this precision may not be enough to determine the amplitude of the resonant argument.

[1] *http://www.cfeps.net/tnodb/*, *http://www.obs-besancon.fr/bdp/*

Table 2. Follow-up/Tracking Observations.

UT Date	Telescope	No. Obs.
2002 Aug 05	CFHT + 12k	6
2002 Sep 03	NOT 2.56m	6
2002 Sep 02	Calar-Alto 2.2-m	9
2002 Sep 30	CFHT 3.5-m	6
2002 Nov 28	CFHT 3.5-m	10
2003 Jul 26	ESO 2.2m	6
2004 Feb 19	WIYN 3.5-m	4
2004 Apr 15	Hale 5-m	73
2004 May 24	Mayall 3.8-m	6
2004 Aug 12	CFHT 3.5m	15
2004 Sep 06	KPNO 2m	15
2004 Sep 11	Mayall 3.8-m	25
2004 Sep 16	Hale 5-m	20
2004 Sep 21	CFHT 3.5m	4
2005 Jul 08	Gemini-North 8-m	45
2005 Jul 09	Hale 5-m	47
2005 Jul 11	ESO 2.2m	25
2005 Aug 01	VLT UT-1	53
2005 Sep 24	WIYN 3.5-m	9
2005 Oct 03	Hale 5-m	72
2005 Nov 04	Mayall 3.8m	31
2005 Dec 04	MDM 2.4-m	10
2006 Jan 28	Hale 5-m	50
2006 May 01	CFHT 3.5m	23
2006 May 02	WIYN 3.5-m	32
2006 May 26	CFHT 3.5m	20
2006 Jun 25	Mayall 3.8-m	2
2006 Jul 03	CFHT 3.5m	18
2006 Jul 26	Hale 5-m	15
2006 Sep 18	CFHT 3.5m	7
2006 Sep 26	MMT 6.5m	11
2006 Oct 22	Hale 5-m	29
2006 Oct 21	WHT 4m	17

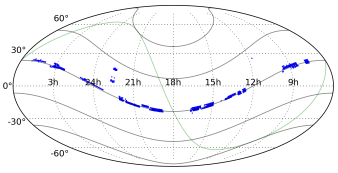

Fig. 1.— Geometry of the CFEPS discovery-blocks. The RA and DEC grid is indicated with dotted lines.

Of the 196 TNOs in our CFEPS characterized sample 169 have been tracked through 3 oppositions or more (ie. not lost) and their orbits are now known to a precision of $\Delta a/a < 0.1\%$ and can be reliably classified into orbital sub-populations (see below). The very high fraction of our characterized sample for which classification is possible (86%) is by far the largest 'tracking fraction' among large scale TNO surveys to-date and is due to the strong emphasis on followup observations in our observing strategy, made possible thanks to the time allocation committees of the many observatories listed in Table 2.

The initial tracking of TNOs discovered by CFEPS is through blind return to the discovery fields to ensure that there is no orbital bias in the tracked fraction. We do find, however, that the tracked fraction is a function of the magnitude of the TNO and have characterized this bias. For the full CFEPS fields we find the same magnitude dependance as for the L3 fields for objects brighter than the limit of the characterized sample, which we model as

$$f_{t,L7}(g) = \begin{cases} 1.0 & (g \leqslant 22.8) \\ 1.0 - 0.25(g - 22.8) & (g > 22.8) \end{cases}$$

where $f_{t,L7}$ is the tracked fraction. The tracked fraction remains well above 50% down to the characterized limit of the survey blocks. We have also re-examined the magnitude dependence of the tracked fraction of our Pre-survey discoveries (Jones et al. 2006) and find

$$f_{t,L7}(g) = \begin{cases} 1.0 & (g \leqslant 24.1) \\ 1.0 - 2.5(g - 24.1) & (g > 24.1) \end{cases} .$$

The Pre-survey observations used much longer exposure times than for CFEPS, hence the deeper limiting magnitude reached. We also had a smaller survey area and were able to perform a more thorough follow-up campaign, resulting in a tracking efficiency that essentially was 100% up to the limiting magnitude of the discoveries. Our Pre-survey discovery observations where reported on the Landolt-R system and we have transformed our Pre-survey limits to g, for use in our survey simulator, using a constant color offset of (g - R) = 0.8 (Hainaut & Delsanti 2002).

4.1. Orbit Classification

We adopt the convention that, based on orbital elements and dynamical behavior, the Kuiper Belt can be divided into three broad orbital classes. An object is checked against each dynamical class in the order below to decide whether or not it belongs to that class, each object can belong to only one class. A schematic representation of this dynamical classifaction is shown in Figure 1 of Gladman et al. (2008).

- resonant (objects currently in a mean-motion resonance with Neptune)
- scattering (objects that over 10 Myr forward in time integrations experience encounters with Neptune resulting in variation of semimajor-axis of more than 1.5 AU)

Table 2—Continued

UT Date	Telescope	No. Obs.
2006 Nov 23	WIYN 3.5-m	41
2007 Feb 14	2.1-m reflector	3
2007 Feb 21	Hale 5-m	22
2007 May 15	Hale 5-m	45
2007 May 15	KPNO 2m	23
2007 Jun 02	MMT 6.5m	3
2007 Sep 11	WIYN 3.5-m	32
2007 Sep 16	Hale 5-m	27
2007 Nov 08	WIYN 3.5-m	30
2008 May 03	WIYN 3.5-m	52
2008 Jun 07	CTIO 4-m	28
2008 Oct 23	WIYN 3.5-m	3
2008 Dec 06	Hale 5-m	9
2009 Jan 26	CFHT 3.5m	19
2009 Apr 17	MMT 6.5m	3
2009 Apr 23	Subaru 8-m	1
2009 Jun 20	WIYN 3.5-m	22

Note. — UT Date is the start of the observing run; No. Obs. is the number of astrometric measures reported from the observing run. Only observations not part of the Very Wide component of CFHT-LS are reported here. Runs with low numbers of astrometric measures were either wiped out by poor weather, or not meant for CFEPS objects follow-up originally.

- classical or detached belt (everything that remains). One further sub-divides the classical belt into:
  - inner classical belt (objects with semi-major axis interior to the 3:2 MMR)
  - main classical belt (objects whose semi-major axis is between the 3:2 and 2:1 MMRs)
  - outer classical belt (objects with semi-major axis exterior to the 2:1 MMR with $e < 0.24$)
  - detached (those objects with semi-major axis beyond the 2:1 MMR that have $e > 0.24$)

The classical belt is often also divided into high-inclination and low-inclination objects. For the L7 model, we work from the hypothesis described in Brown (2001) that there exist two distinct populations, one with a wide inclination distribution (the 'hot' population), and the other one with a narrow inclination distribution (the 'cold' population), with both populations overlapping with each other in inclination space (thus some "cold" objects may have large inclination, and some "hot" objects may have low inclination). In the literature, the separation between hot and cold populations is sometimes presented as a sharp cut in inclination, often around 5°, under the assumption that an object with inclination less (greater) than that threshold has a very high likelihood to be a member of the cold (hot) population. As will be seen in Section 5.1.1, the veracity of this assumption depends on the physical size of the objects being sorted, larger objects (H <7) having a much higher probability of being from the hot population, regardless of their inclination, while the objects from the cold population dominate at smaller (H>8) sizes. A strict inclination cut does not isolate the two mixed populations.

Following the procedure in Gladman et al. (2008) (similar to Chiang et al. 2003b), we extend the L3 sample classification given in P1 to our full CFEPS sample as of November 2009 (including all refinement observations to that date). Using this classification procedure, 15 of our objects remain insecure (even though these have observational arcs extending across 5 oppositions!); all of these are due to their proximity to a resonance border where the remaining astrometric uncertainty makes it unclear if the object is actually resonant. We list these 'insecure' objects in the category shown by 2 of the 3 clones. Table 3 gives the classification of all characterized objects used for comparison with the Survey Simulator's artificial detections. Several objects had been independently discovered before we submitted our observations to the MPC and are marked with a PD suffix. Although we do not claim 'discoverer credit' for these objects, they have just as much scientficially-exploitable value because they were detected during our characterized observations and hence can to be included when running our survey simulator. Table 4 gives the classification of the tracked objects below the 40% efficiency threshold, hence deemed non-characterized and not used in our Survey Simulator comparisons.

Table 3. Characterized Object Classification.

DESIGNATIONS		a	e	i	dist		Comment
CFEPS	MPC	AU		°	AU		
			Resonant Objects				
L3y11	(131697) 2001 XH255	34.925	0.0736	2.856	34.0	5:4	MPC_W
L4h14	2004 HM79	36.441	0.07943	1.172	38.0	4:3	
L3s06	(143685) 2003 SS317	36.456	0.2360	5.905	28.2	4:3	
L5c23	2005 CF81	36.473	0.06353	0.405	34.4	4:3	
L7a10	2005 GH228	36.663	0.18814	17.151	30.6	4:3	I
L4k11	2004 KC19	39.258	0.23605	5.637	30.2	3:2	
L4h15	2004 HB79	39.260	0.22862	2.661	32.0	3:2	
L5c11	2005 CD81	39.262	0.15158	21.344	45.2	3:2	
L4h06	2004 HY78	39.302	0.19571	12.584	31.8	3:2	
L4v18	2004 VY130	39.342	0.27616	10.203	28.5	3:2	
L4m02	2004 MS8	39.344	0.29677	12.249	27.8	3:2	
L3s02	2003 SO317	39.346	0.2750	6.563	32.3	3:2	
L4h09PD	(47932) 2000 GN171	39.352	0.28120	10.815	28.5	3:2	
L3h19	2003 HF57	39.36	0.194	1.423	32.4	3:2	
L3w07	2003 TH58	39.36	0.0911	27.935	35.8	3:2	
L4h07	2004 HA79	39.378	0.24697	22.700	38.4	3:2	
L3h11	2003 HA57	39.399	0.1710	27.626	32.7	3:2	
L3w01	2005 TV189	39.41	0.1884	34.390	32.0	3:2	
L4j11	2004 HX78	39.420	0.15270	16.272	33.6	3:2	
L4v09	2004 VX130	39.430	0.20696	5.745	34.8	3:2	
L3h14	2003 HD57	39.44	0.179	5.621	32.9	3:2	
L3s05	2003 SR317	39.44	0.1667	8.348	35.5	3:2	
L4v13	2004 VV130	39.454	0.18827	23.924	32.8	3:2	
L4k01	2004 KB19	39.484	0.21859	17.156	39.5	3:2	
L3h01	2004 FW164	39.492	0.1575	9.114	33.3	3:2	
L5i06PD	2001 KQ77	39.505	0.15619	15.617	36.2	3:2	
L4h10PD	1995 HM5	39.521	0.25197	4.814	31.1	3:2	
L4v12	2004 VZ130	39.551	0.28159	11.581	29.2	3:2	
L4h08	2004 HZ78	39.580	0.15095	13.310	34.8	3:2	
L5c08	2006 CJ69	42.183	0.22866	17.916	35.5	5:3	
L3y06	2003 YW179	42.193	0.1537	2.384	35.7	5:3	
L5c13PD	1999 CX131	42.240	0.23387	9.757	41.8	5:3	
L4v05	2004 VE131	42.297	0.25889	5.198	39.6	5:3	
L3y12PD	(126154) 2001 YH140	42.332	0.14043	11.078	36.4	5:3	
L4k10	2004 KK19	42.410	0.14391	4.485	46.0	5:3	I
L3q08PD	(135742) 2002 PB171	43.63	0.125	5.450	40.7	7:4	
L4n03	2004 OQ15	43.646	0.12472	9.727	40.5	7:4	
L3w03	2003 YJ179	43.66	0.0794	1.446	40.3	7:4	

Table 3—Continued

DESIGNATIONS CFEPS	DESIGNATIONS MPC	a AU	e	i °	dist AU	Comment	
L4v10	2004 VF131	43.672	0.21492	0.816	42.0	7:4	
K02O03	2000 OP67	43.72	0.19 1	0.751	39.3	7:4	
L4h11	2004 HN79	45.736	0.22936	11.669	37.4	15:8	I
L4h18	2004 HP79	47.567	0.18250	2.253	39.5	2:1	
L4k16	2004 KL19	47.660	0.32262	5.732	32.3	2:1	
L4k20	2004 KM19	47.720	0.29180	1.686	33.8	2:1	
K02O12	2002 PU170	47.75	0.2213	1.918	47.2	2:1	
L4v06	2004 VK78	47.764	0.33029	1.467	32.5	2:1	
L3y07	(131696) 2001 XT254	52.92	0.3221	0.518	36.6	7:3	MPC_W
L5c19PD	2002 CZ248	53.039	0.38913	5.466	36.2	7:3	
L5c12	2002 CY224	53.892	0.34651	15.733	36.3	12:5	
L4j08	2004 HO79	55.206	0.41166	5.624	37.3	5:2	
L3f04PD	(60621) 2000 FE8	55.29	0.4020	5.869	36.0	5:2	
L4j06PD	2002 GP32	55.387	0.42195	1.559	32.1	5:2	
L4k14	2004 KZ18	55.419	0.38191	22.645	34.4	5:2	
L4h02PD	2004 EG96	55.550	0.42291	16.213	32.2	5:2	
L4v08	2004 VU130	62.194	0.42806	8.024	49.7	3:1	
L3y02	2003 YQ179	88.38	0.5785	20.873	39.3	5:1	I
		Inner Classical Belt					
L3y14PD	(131695) 2001 XS254	37.220	0.05211	4.262	35.3	I (11:8)	
L4q12PD	2000 OB51	37.820	0.03501	4.458	36.6		
L4q10	1999 OJ4	38.017	0.02539	4.000	38.1		
L4k18	2004 KD19	38.257	0.01707	2.126	38.9		
L4o01	2004 OP15	38.584	0.05532	22.946	38.7		
L3w06	2003 YL179	38.82	0.002	2.525	38.7		
		Main Classical Belt					
L4k12	2004 KH19	40.772	0.11721	35.230	43.6		
L4q05	2004 QE29	40.878	0.08372	24.125	37.5		
L4k19	2005 JB186	41.471	0.10588	20.220	38.0		
L3w05	2003 YK179	41.67	0.146	19.605	42.7		
L4h16	2004 HL79	42.126	0.07520	16.759	40.0		
L5s01PD	(120347) 2004 SB60	42.028	0.10667	23.931	43.7		
L3s01	2003 SN317	42.50	0.0421	1.497	41.5		
L4q15	1999 ON4	42.571	0.03995	3.187	40.9		

Table 3—Continued

DESIGNATIONS		a	e	i	dist	Comment
CFEPS	MPC	AU		°	AU	
L3h05	2003 HY56	42.604	0.037	2.578	42.5	
L3q02PD	2001 QB298	42.618	0.0962	1.800	39.1	
L3s03	2003 SQ317	42.63	0.0795	28.568	39.3	
K02O20	2002 PV170	42.643	0.016	1.271	42.2	
K02P32	2002 PX170	42.65	0.041	1.570	42.8	
L5c03	2005 CE81	42.715	0.04666	3.084	40.8	
L5i01	2006 HA123	42.778	0.04615	3.303	41.0	
L4p02	2004 PU117	42.817	0.01461	1.874	42.4	
L4p01	2004 PT117	42.983	0.04115	1.238	43.6	
K02O40	2002 PY170	43.015	0.030	3.016	43.0	
L4q03	2004 QD29	43.020	0.11388	23.862	40.6	I (12:7)
L3w11	2003 TK58	43.078	0.0647	3.355	45.6	
L4m03	2004 MT8	43.120	0.04195	2.239	44.9	
L4h05PD	2001 FK185	43.255	0.03994	1.171	41.7	
L4j10	2004 HH79	43.259	0.06010	8.610	43.2	
L4j02	2004 HF79	43.269	0.02547	1.484	42.4	
L4k04	2004 KG19	43.272	0.02164	0.963	42.4	
L5c07PD	2005 XU100	43.398	0.10283	7.869	41.7	
L7a06	2006 WF206	43.500	0.04246	2.056	44.4	
L3w10	2003 TL58	43.542	0.0456	7.738	42.2	
L3y01	2003 YX179	43.582	0.044	4.850	42.5	
L3y05	2003 YS179	43.585	0.022	3.727	43.8	
L3h18	2003 HG57	43.612	0.0323	2.098	43.0	
L4p05	2004 PW117	43.620	0.06023	1.862	46.0	
L7a05	2005 BV49	43.684	0.04575	7.981	41.8	
L5j04	2005 LB54	43.690	0.04752	3.006	41.8	
L4h01PD	(181708) 1993 FW	43.717	0.04807	7.750	41.9	
L4p06PD	2001 QY297	43.835	0.08332	1.547	42.8	
L4h12	2004 HK79	43.888	0.07800	1.946	41.3	
L5i03PD	2001 KO77	43.898	0.14569	20.726	37.7	
L4h13	2004 HJ79	43.947	0.04419	3.317	45.0	
L4v03	2004 VC131	43.951	0.07395	0.490	40.7	
L5c22	2007 DS101	43.991	0.08474	1.389	44.6	
L3h13	2003 HH57	44.04	0.088	1.436	40.2	
L3h09	2003 HC57	44.05	0.072	1.038	43.4	
L5i05	2005 JY185	44.077	0.06848	2.139	44.6	
L7a07	2005 BW49	44.097	0.07959	2.102	41.9	
L3q06PD	2001 QJ298	44.10	0.0388	2.151	45.2	
L4k03	2004 KF19	44.123	0.06348	0.108	41.4	
L5c21PD	2005 EE296	44.126	0.06804	3.296	46.2	
L3q09PD	2001 QX297	44.15	0.0275	0.911	43.5	
L5c18	2007 CS79	44.159	0.03582	1.540	42.8	
L3h20	2003 HE57	44.17	0.100	8.863	40.0	
L5c24PD	1999 CU153	44.172	0.06520	2.698	42.7	
L4v02	2004 VB131	44.189	0.07267	1.747	46.5	

Table 3—Continued

DESIGNATIONS CFEPS	DESIGNATIONS MPC	a AU	e	i °	dist AU	Comment
L4j03	2004 HG79	44.200	0.02298	3.595	43.2	
L4p09	2004 PX117	44.261	0.09965	3.747	46.1	
L4p08PD	2001 QZ297	44.283	0.06442	1.856	42.0	
L5j03	2005 LA54	44.314	0.06719	7.919	41.6	
L4j01	2004 HE79	44.316	0.09805	3.089	40.0	
K02P41	2002 PA171	44.34	0.076	2.511	47.7	
L4k02	2004 KE19	44.360	0.04981	1.178	42.6	
L3w08	2003 TJ58	44.40	0.0864	0.954	40.8	
L3w02	2003 TG58	44.54	0.103	1.660	43.7	I (9:5)
L3w04	(143991) 2003 YO179	44.602	0.1370	19.393	41.3	
L5i08	2005 JJ186	44.636	0.09431	4.141	41.8	
K02O43	2002 PC171	44.706	0.059	3.574	42.7	
L4n04	2004 MU8	44.856	0.08180	3.580	48.2	
K02O32	2002 PW170	44.88	0.074	3.933	47.4	
L4q16	(66452) 1999 OF4	44.933	0.06380	2.660	45.2	
L4j12	2006 JV58	44.961	0.06094	0.317	42.2	
L5c20PD	2002 CZ224	44.980	0.06304	1.687	47.7	I (11:6)
L3w09	2004 XX190	45.171	0.1042	1.577	40.9	
L5c10PD	1999 CJ119	45.325	0.06651	3.205	42.3	
L5c06	2007 CQ79	45.441	0.07721	1.185	45.8	
L4v01	2004 VA131	45.538	0.09613	0.767	41.2	
L4k15PD	2003 LB7	45.580	0.13130	2.294	40.1	
L5c02	2006 CH69	45.735	0.03535	1.791	44.2	
L4q11	1999 OM4	45.924	0.11643	2.088	44.0	
L4j07	2004 HD79	45.941	0.03205	1.305	47.3	
L5i02PD	2001 KW76	46.013	0.21613	10.460	39.6	
L4p03	2004 PV117	46.069	0.15343	4.324	39.5	
L7a04PD	2002 CY248	46.191	0.14635	7.038	51.8	
L4k13	2006 JU58	46.239	0.12464	7.035	46.5	
L3q04PD	2002 PT170	46.24	0.143	3.703	50.5	
L4v14	2004 VD131	46.324	0.12253	3.646	41.5	
L4j05	2004 HC79	46.399	0.16064	1.446	39.0	
L4q09	2000 PD30	46.519	0.02232	4.594	45.7	
L3y03	2003 YU179	46.75	0.1597	4.855	39.6	
L4k17	2004 KJ19	46.967	0.23543	24.421	38.5	
L7a11PD	2000 CO105	47.046	0.14750	19.270	49.3	
L3y09	2003 YV179	47.10	0.222	15.569	41.1	
L5c14	2007 CR79	47.149	0.21876	21.869	36.9	
L3h04	2003 HX56	47.196	0.2239	29.525	45.5	
L4m04	2004 MV8	47.234	0.17503	27.205	39.1	
		Outer Classical Belt				
L4q06	2004 QG29	48.480	0.23517	27.134	37.8	
L4q14	2004 QH29	50.859	0.22922	12.010	39.9	

121 (64%) of the tracked sample are in the classical belt, split into 6 (3%) inner, 101 (54%) main, 3 (2%) outer and 11 (6%) detached belt objects. Orbital integration shows that 58 (31%) objects are in a mean-motion resonance with Neptune, 25 (13%) of which are plutinos. The remaining sample consists of 9 (5%) objects on scattering orbits.

The apparent motion of TNOs in our opposition discovery fields is approximately $\theta(''/\mathrm{hr}) \simeq (147\ \mathrm{AU})/r$, where r is the heliocentric distance in AU. With a typical seeing of 0.7 - 0.9 arc-second and a timebase of 70 - 90 minutes between first and third frames, we were sensitive to objects as distant as $r \simeq 125$ AU, provided they are large enough to be above our flux limit. The furthest object discovered in CFEPS lies at 58.3 AU from the Sun (L3q03 = 2003 QX_{113}, a detached object with $a = 49.55$ AU). The short exposure times used (70 - 90 seconds) allowed us to detect objects as close as 15 AU without trailing. We elected to use a rate of motion cut corresponding to objects further than 20 AU from Earth.

In the following sections we present a parameterization of the intrinsic classical Kuiper belt and scattering disk population implied by our observations. The differing detectability of these populations, in a flux-limited survey, implies that the intrinsic population ratios will be different from the observed ones. We present the more complex analysis of the resonant populations in a companion paper (Gladman et al. 2011).

5. The classical belt's orbital distribution

This section presents the results of our search for an empirical parameterized orbit distribution for the various components of the so-called 'classical' belt. For each sub-component we start with a simple parameterization of the intrinsic orbit and absolute magnitude distributions. We then use the CFEPS Survey Simulator[2] to determine which members of the intrinsic population would have been detected by the survey. The orbital-element distributions of the simulated detections are then compared to our characterized sample. This process is iterated with models of increasing complexity until arriving at a model that provides a statistically-acceptable match; no cosmogonic considerations are invoked.

Our model search process provided acceptable parameterizations of the main classical belt, the inner classical belt and the outer+detached population. Our goal is to discover the main features of the orbital distribution and provide a population estimate for each orbital sub-component. While our success in finding acceptable models is not a proof of model uniqueness, we were surprised, in many cases, by the restricted range of acceptable models.

To evaluate a model's quality, we extend the method defined in P1 to more variables. We compute the Anderson-Darling (AD) (Information Technology Laboratory 2011) statistic for the distributions of the orbital elements a, e, i, q, and for r (heliocentric distance at discovery) and g magnitude. We use Kuiper's modified Kolmogorov-Smirnov (KKS) statistic for the mean anomaly M. We follow the same procedure as

[2]The survey simulator is available on-line, with all informations needed to use it, at *http://www.cfeps.net* as a stand-alone package, or at *http://CFEPSSim.obs-besancon.fr/*, as an on-line service.

Table 3—Continued

DESIGNATIONS CFEPS	DESIGNATIONS MPC	a AU	e	i °	dist AU	Comment
L5c16	2005 CG81	53.834	0.23684	26.154	44.6	
		Detached Classical Belt				
L5i04	2005 JK186	47.264	0.24363	27.252	38.1	
L3q03	2003 QX113	49.55	0.252	6.753	58.3	
L7a02	2006 WG206	50.416	0.29111	14.297	38.9	
L4p04PD	2000 PE30	54.318	0.34216	18.416	37.6	
L5c15	2005 CH81	55.156	0.31812	5.136	37.6	
L4n06	2004 OS15	55.760	0.31667	4.248	39.5	
L4n05	2004 OR15	56.248	0.33882	6.919	37.3	
L3f01	2003 FZ129	61.71	0.3840	5.793	38.0	
L4h21	2004 HQ79	63.299	0.42264	6.473	36.6	
L5j02	2005 LC54	67.354	0.46279	22.443	43.1	I (10:3)
L5r01	2005 RH52	153.800	0.74644	20.447	39.0	I scattering
		Scattering Disk				
L4k09	2004 KV18	30.192	0.18517	13.586	26.6	
L4m01	2004 MW8	33.479	0.33308	8.205	31.4	
L4p07	2004 PY117	39.953	0.28088	23.545	29.6	
L3q01	2003 QW113	50.99	0.484	6.922	38.2	
L7a03	2006 BS284	59.613	0.43949	4.575	47.0	
L4v11	2004 VH131	60.036	0.62928	11.972	26.8	
L4v04	2004 VG131	64.100	0.50638	13.642	31.8	
L3h08	2003 HB57	159.6	0.7613	15.499	38.4	

Note. — M:N: object in the M:N resonance; I: indicates that the orbit classification is insecure (see Gladman et al. (2008) for an explanation of the exact meaning); (M:N): object may be in the M:N resonance; MPC_W: indicates object was in MPC database but found $+1^\circ$ from predicted location. Objects prefixed with *L* are the characterized, tracked objects discovered during CFEPS; objects prefixed with *K02* were discovered in our pre-survey (Jones et al. 2006); The full orbital elements are available in electronic form from either *http://www.cfeps.net/tnodb/* or the MPC.

Table 4. Non Characterized Object Classification.

DESIGNATIONS CFEPS	DESIGNATIONS MPC	a AU	e	i °	dist AU	Comment
		Resonant Objects				
U5j06		39.369	0.22055	13.525	31.2	3:2
U3s04	2003 SP317	45.961	0.1694	5.080	44.9	17:9 I
U7a08		47.702	0.19600	7.020	38.4	2:1
U5j01PD	(136120) 2003 LG7	62.157	0.47825	20.104	33.1	3:1
		Main Classical Belt				
U3w13	2003 YM179	40.960	0.056	23.414	40.2	
U3f02	2003 FA130	42.602	0.031	0.288	41.3	
U4j09		42.642	0.00775	3.044	42.3	
U7a09		42.701	0.09231	2.931	44.8	
U3w17	2002 WL21	43.103	0.0415	2.552	41.6	
U3y16	2003 YR179	43.421	0.0523	9.823	41.3	
U3y04	2003 YT179	43.542	0.028	1.684	44.4	
U3h06	2003 HZ56	43.63	0.010	2.550	43.5	
U5c17PD	1999 CN119	43.733	0.04043	0.999	44.5	
U4n01		43.915	0.13500	0.271	43.7	
U3y08	2003 YP179	44.03	0.079	0.947	41.3	
U4n02		44.056	0.06176	2.943	46.8	
U3w16	2003 YN179	44.272	0.006	2.768	44.4	
U4j04PD	2000 JF81	46.117	0.10218	1.742	44.9	
		Scattering Disk				
U7a01		42.621	0.16444	4.742	38.9	I (5:3)

Note. — $M : N$: object in the M:N resonance; I: indicates that the orbit classification is insecure (see Gladman et al. (2008) for an explanation of the exact meaning).

used in P1 to determine the significance of the computed statistics. For each model parameterization we use the Survey Simulator to draw a large 'parent' population from the model. We then draw sub-samples with the same total number as in our L7 characterized sample. Using this simulated 'observed' population we compute the various statistics that result from comparing to our large 'parent' population. This re-sampling is repeated 5000 times providing a distribution of statistic values for the given parameterization, ie. 'bootstrapping' the statistic. The probability of statistic measured for the L7 sample is determined by comparing that statistic value to the range of statistic values returned by the bootstrap process. We reject a model if the minimum statistical probability determined in this way is returned by fewer than 5% of the model bootstraps.

5.1. The main classical belt

In P1 we presented a model that matched the orbital distribution of the main classical belt objects detected in the L3 sample; due to the smaller number of objects in the L3 sample, we restricted ourselves to fit only selected orbital elements and considered a constrained range of the phase-space volume available to main-classical belt objects. In addition, P1 did not attempt to determine the absolute magnitude distribution using our detections but instead utilized values available in the literature. Here we restrict our main classical belt model to the 40 AU $\leq a \leq$ 47 AU range, to avoid the complex borders of the 3:2 and 2:1 MMR regions, which includes 88 characterized CFEPS TNOs. This sample size allowed us to remove external constraints on the magnitude distribution and explore a more complete model of the available phase-space.

Figures 2 and 3 present (a, i), (a, q) and (i, q) projections of the main-belt TNO orbital elements for characterized CFEPS detections and multi-opposition orbits in the MPC. These figures make it clear that objects with $q < 39$ AU are dominantly from the high-inclination population, as was already apparent in the L3 model. The distribution of low-i objects, which span a narrower range of semimajor axis than their high-i cousins, exhibit considerable phase space structure. In an effort to find a parameterization that yielded these interesting sub-structures we investigated a substantial range of empirical representations. We were, however, unable to find a two-component model (like that in P1) that sufficiently reproduced structure observed in the current sample. A more complex representation is required.

After much effort we arrived at our 'L7 model' (based on CFEPS discoveries up to mid-2007). The L7 model is composed of three components (Fig. 4), the fine details of which are presented in Appendix A. These components are a population with a wide inclination distribution (the *hot* population) superposed on top of a population with narrow inclination component with two semi-major axis / eccentricity distributions (the *stirred* and *kernel* populations). The hot population is defined as a band in perihelion distance q essentially confined to the range 35 to 40 AU, with soft exponential decay outside this range. Using a 'core' (Elliot et al. 2005) definition based only on inclination does not take into account the transition in the e/i distribution beyond $a \simeq$44.4 AU clearly visible in both Figs. 2 and 3. With the qualifier that there will be mixing from the low-i tail from the hot component, we thus split the 'cold' population of the main classical belt into two sub-components. The *stirred* population have orbits drawn from a narrow-inclination distribution with semi-major axes starting at a=42.5 AU and extending to $a \simeq 47$ AU, with a range of eccentricities

that increases as one goes to larger a. The stirred component does not contain the sharp density change at $a \simeq 44.5$ AU. There are more low-i and moderate-e TNOs per unit semimajor axis at $a \sim 44 - 44.5$ AU than at smaller and larger semi-major axis, indicating that a third component is required. To model this component we insert a dense low-inclination concentration, which we call the *kernel*, near a=44 AU to account for this intrinsic population.

The kernel may be the same as the clustering in the a =42–44 region seen as far back as Jewitt & Luu (1995) and Jewitt et al. (1996). This also appears to be the same structure that Chiang (2002) and Chiang et al. (2003a) posited (with rightful skepticism) as a possible collisional family. Although we share the concern that normally the relative speeds from a large parent-body breakup should be larger than this clump's observed dispersion, we find that regardless of interpretation, there is considerable observational support for a tightly-confined structure in orbital element space near the location Chiang et al. pointed to. Recent collisional modeling studies (eg. Leinhardt et al. 2010) raise the possibility of grazing impacts forming low-speed families in the Kuiper Belt, motivated by the Haumea family (Brown et al. 2007). The large number of $D \geq 170$ km (absolute magnitude[3] $H_g \leq 8$) objects in the kernel implies that the parent body would have been a dwarf planet at least as large as Pluto, an unlikely possibility. The kernel thus appears to be the longest-recognized dynamical sub-structure in the classical Kuiper Belt, a structure which requires confinement in all of a, e, and i.

There may be other possible representations of the orbital distribution that are consistent with the CFEPS detections, with different boundaries or divisions of the phase space. We have found, however, the generic necessity of a 3-component model can not be avoided. The main characteristics of our model must be similar to reality, because a considerable amount of tuning was needed to achieve an acceptable model. From this 3-component model, we can then provide robust measurements of the sizes of the subpopulations in the Kuiper belt and generate a synthetic 'de-biased' model of the orbital distribution of the main belt which can be used for various modeling purposes, such as collisional dust production (Stark & Kuchner 2010).

5.1.1. The luminosity function

The absolute magnitude H_g distribution can be represented by an exponential function

$$N(\mathrm{H}) \propto 10^{\alpha \mathrm{H}}$$

with 'slope' α. H_g is converted into apparent magnitude g by $g = H_g + 2.5 \log(r^2 \Delta^2 \Phi(\mu))$, where Δ is the geocentric and r the heliocentric distance, μ the phase angle (Sun-TNO-observer) and $\Phi(\mu)$ the phase function defined by Bowell et al. (1989). We find that two different values of α, one for the hot and one for the cold distributions, are required by our observations. Allowing the stirred and kernel components to have differing values of α did not provide an improved match to the observations and is not required.

[3]The g-band apparent magnitude of a TNO at heliocentric and geocentric distance of 1 AU if viewed at 0° phase angle

We have run a series of model cases using the orbital element distributions described previously while varying the luminosity functions slopes for the hot component, α_h, and for the cold (kernel + stirred) components α_c. For each case, we varied the other orbit model parameters to find the best possible match between the cumulative distribution functions of the Survey Simulator observed Kuiper belt and the L7 sample for each of the selected values of α_h and α_c. In this way we determined the range of allowed power-law slopes for the limited range of TNO sizes, $7 \lesssim H_g \lesssim 8$, probed by our observations.

Our best fit values are $\alpha_c = 1.2^{+0.2}_{-0.3}$ and $\alpha_h = 0.8^{+0.3}_{-0.2}$, with Fig. 5 presenting the joint 95% confidence region for these slopes. A single value of α for all sub-components in our model is rejected at >99% confidence. The α_c determined here is in good agreement with the range derived by Bernstein et al. (2004) for the low-inclination objects and somewhat steeper than that reported in Elliot et al. (2005) while our value for α_h overlaps the ranges proposed by both Bernstein et al. (2004) and Elliot et al. (2005) for what they call the excited population. Fraser et al. (2010) also found markedly different values for the slope of the cold component, 0.59–1.05, and the hot component, 0.14–0.56. While those slopes are consistent with Elliot et al. (2005) they are shallower than Bernstein et al. (2004) and our own estimates. The Fraser et al. (2010) results, however, probed smaller-size objects than our observations and the difference in slopes may be reflective of a change in size distribution around $H \sim 8.5$ where the CFEPS detections dwindle. Thus, in the limited size ranges probed by these surveys, there appears to be reasonable agreement on the slope of luminosity function for these components of the Kuiper belt with the hot and cold components exhibiting slopes that are significantly different.

The value of size distribution slopes reported here range from 0.8–1.2 and are considerably larger than the best-fit slopes discussed in many previous analyses that attempted to determine a global luminosity function for the Kuiper belt. For example, Petit et al. (2008) reviewed estimates of α ranging from 0.5–0.8 for surveys that cover the range $H_g \simeq$5–10. Fraser & Kavelaars (2009) and Fuentes et al. (2009) demonstrated that a slope of $\sim \alpha = 0.75$ is a decent representation of the 'average' belt down to magnitude $\sim m_r$=25, but that there is a gradual flattening of the apparent luminosity-function slope at fainter magnitudes, continuing to a slope which may become extremely flat somewhere beyond $H > 10$ according to the Bernstein et al. (2004) analysis of a deep HST search. The quest for a single 'master' luminosity function, however, is misguided:

1. Because there are different slopes for the hot and cold main-belt components, the slope should be $\alpha \simeq$0.8 at large sizes (where the hot component dominates) and become steeper (if looking in the ecliptic where the cold population is visible) when the depth of the survey results begins to probe the size range at which the cold-population surface density becomes comparable to the hot population.

2. The on-sky density of the (essentially non-resonant) cold population is essentially dependent only on the ecliptic latitude. The hot population's sky density varies with both latitude and longitude due to the fact that the resonant populations are hot. Thus, the H magnitude at which the steeper cold component power-law takes over will also depend on the latitude and longitude of the survey.

Interestingly, extrapolating from the ∼4000 objects in the cold belt with $H_g \leq$8 (see sect. 5.1.3) to

larger objects, one finds that there should be only ∼1 TNO with H_g <5. This is consistent with the current census of large objects in the cold belt, which should be close to complete (Trujillo & Brown 2003). Similarly, one would expect to have only ∼1 TNO with H_g <3.5 in the non-resonant hot population, which again corresponds to our knowledge of the Kuiper belt (Brown 2008). Currently, the MPC report 6 objects with absolute magnitude <3.5 in the classical belt region as defined for our population estimate. 5 of them are clearly part of the hot population, with inclinations between 20 and 30 degrees, the last one being Quaoar with an intermediate inclination of 8 degrees.

The realization that the hot component has a low-i tail means that caution must be exercised because one simply cannot isolate the 'cold' cosmogonic population with the commonly-used $i < 5^\circ$ cut. For example, in the ecliptic at bright (say roughly $m_r \sim 22$) magnitudes, the low-i tail of the hot component can be numerically comparable to the sky density of 'cold' objects. Thus, it is not possible to isolate the cold component at bright magnitudes based simply on orbital inclination.

5.1.2. Acceptable range for main parameters.

In this section we fix the slopes just determined, i.e. $\alpha_h = 0.8$ and $\alpha_c = 1.2$ and examine the range of model parameters allowed by the L7 detections. Due to the large number of orbital parameters to adjust and the time required by each survey simulation (10–50 minutes on the fastest available computers), we did not run an automated minimum-finding algorithm, but rather did a manual search on a multidimensional parameter grid.

Acceptable values (rejectable at less than 95% confidence) for the inclination width (see Appendix A) of the hot component σ_h range from 14°–29°. A hot-component width $\sigma_h = 16^\circ$ is acceptable not just for the main-belt population but also reproduces the observed inner and outer classical populations (see Sections 5.2 and 5.3) and thus we adopt this value as the width of hot component.

The acceptable range for σ_c is 2.3°-3.5°, with a peak of the probability near 2.6°, which we adopt. Brown (2001) analysed the MPC database at the time and concluded the existence of the cold component to the inclination distribution; with $\sigma_c = 2.2^{+0.2}_{-0.6}$ degrees (one-sigma uncertainties), consistent with our results. Elliot et al. (2005) in their initial analysis of the Deep Ecliptic Survey estimated a 1.94 ± 0.19-degree width for the cold component. Gulbis et al. (2010), however, recently re-analysed the detections from the Deep Ecliptic Survey, and found a $2.0^{+0.6}_{-0.5}$-degree width (one-sigma uncertainties) for the cold component. Thus, the DES is also in reasonable agreement with our results, given the uncertainties. Brown & Pan (2004) found a much narrower width of 1.3° (no uncertainty given) for the cold component, with respect to a locally-determined Laplace plane for each semimajor axis. We have not repeated a similar analysis.

The L7 distribution contains an excess of intermediate-inclination objects (i in range 6°–10°) when compared to models with $\sigma_h \geq 16^\circ$ and $\sigma_c = 2.2^\circ$. This 'bump' in the cumulative inclination distribution can also be seen in the DES sample, Millis et al. (2002, Fig. 13) and Elliot et al. (2005, Fig. 17), between inclinations of 8° and 10°. The Survey Simulator approach accounts for the distributions of all orbital elements simultaneously and thus the L7 model makes the inclination bump part of the cold component

because the objects in this inclination range have e and a distributions that make them part of the cold component, hence increasing its width. Although it was possible to keep a cold width of 2.2° or lower by introducing a third inclination component the observations do not currently demand this increase in complexity.

The observed cumulative inclination distribution has two steep increases corresponding to the cold and hot component, both of which are steeper than for our model. This indicates that the actual differential distribution of each component is probably more confined than $\sin(i)$ times a Gaussian centered on zero. It is remarkable that the hot component of the main classical belt extends up to 35° and stops abruptly. This limit is seen not only in the CFEPS, but also in the MPC databases (see Figures 2 and 3). We experimented with $\sin^2(i)$ times a Gaussian centered on zero, but this did not result in a significant improvement to our fit. Note that Elliot et al. (2005) find that $\sin(i)$ times a Gaussian plus Lorenzian give their best fit to the classical belt inclination distribution. More recently, Gulbis et al. (2010) find that $\sin(i)$ times a Gaussian of width $\sim 7°$ and centered around $\sim 20°$ best fits what they call the 'Scattered Object' inclination distribution. We did not test this functional form as this introduces an extra parameter, which is not demanded by the current sample. The Brown (2001) functional form may not be an exact representation of every sub-component's inclination distributions; we can, however, obtain an acceptable match to the CFEPS survey with this functional form.

The fraction of each component (hot versus cold inclination components) varies with the H_g-magnitude limit, due to their differing values of α. We report here the acceptable range for the fractions of each sub-population at the $H_g \leq$8.0 limit. We find that the fraction of the hot component, f_h, cannot exceed 62% and is at least 33%, with a best match to the observations at $f_h \simeq 0.51$. This hot-component fraction and widths are close to the nominal L3 model from P1. We find that the fraction of the kernel f_k has to be larger than 0.05, but less than 0.30 at 95% confidence and adopt $f_k = 0.11$. The fraction in the stirred is then f_s=0.38, when considering $H_g < 8.0$.

Figure 6 presents the comparison of our nominal model with a, e, i and g apparent-magnitude distributions. When biased by the CFEPS survey simulator, the L7-model reproduces the detections extremely well.

Our hot/cold population fractions differ from those reported in some other works, but details are important in the comparison. Brown (2001) report a hot fraction of 81%. This fraction listed must be treated with the caution engendered by the realization that the MPC sample has a non-uniform H-magnitude limit, making interpretation of a fractional population (given the different luminosity functions) difficult. The Gulbis et al. (2010) estimate is even more difficult to compare, because the classification scheme used explicitly separates out many of the highest-inclination main-belt TNOs into portions of the 'scattered' population (even though many of these TNOs are very decoupled from Neptune) and thus the relatively small 'hot' width of 8^{+3}_{-2} has been forced down; a direct comparison of the relative populations is thus not possible. Trujillo et al. (2001) has a H-magnitude limit that is more uniform than the MPC sample but they mix together the various orbital classes when reporting the relative fraction of hot and cold component objects.

5.1.3. Population Estimates

The procedure in Section 4.3 of P1 was used to derive a population estimate for the main classical belt. Unlike much of the literature, which gives population estimates for objects larger than an estimated diameter, CFEPS gives population estimates for absolute magnitude smaller than a given value of H_g, and thus an unknown albedo is not introduced into the estimate[4]. These estimates and their uncertainties are given assuming our orbital model. They would change if we were to change our parameterization. In particular, increasing the width of the inclination distributions 'hides' more of the population far from the ecliptic. Alternately, decreasing the cold component's width to 1.3° requires changing the hot/cold fraction and results in a decrease of the total main-belt population by 20%.

In principle, the very deepest blocks in our survey are sensitive to a limit of $H_g \simeq 9.5$ for a perihelion detection on the most eccentric orbits in our main-belt model. The Survey Simulator shows, however, that based on our model orbit distribution, the vast majority of our detections should have $H_g \leq 8.0$, consistent with our largest-H classical-belter detection, $H_g = 8.1$. Thus our population estimate is given to the limit to which the survey has reasonable sensitivity:

$$N_{\rm classical}(H_g \leq 8.0) = (8000^{+1800}_{-1600})$$

where the uncertainties reflect a 95% confidence limit assuming the underlying orbital model and its parameter values are correct. Our measured value for α essentially is only for the range $H_g = 7$–8 which dominate our detections.

The formula

$$N(H_g \leq H_1) = 10^{\alpha \times \Delta H} N(H_g \leq H_0) \ ,$$

where $\Delta H = H_1 - H_0$, allows one to scale population estimates of P1 to $H_g = 8.0$, and also compare with other populations like the inner belt or the plutinos (which can come closer to Earth than the main classical belt). Here care must be taken to distinguish between the hot components and the others because they have different H-magnitude slopes, hence the extrapolation factor to any particular H-limit is different for each sub-component. Figure 7 shows a schematic representation of the fractional population sizes of all the dynamical classes measured in the L7 model. This figure demonstrates that one must be careful when comparing the relative sizes of various sub-populations whose size-distributions are different because the relative populations will vary with the H-magnitude limit being considered.

Due to the lack of phase relations with Neptune and good statistics due to large numbers of main-belt detections in ecliptic surveys, the main classical-belt population estimates should be the most certain in the literature of all the populatoin estimates. Comparing the L7 main-belt estimate with the literature yields satisfactory agreement (details are given in Appendix C). Table 5 provides our current population estimates, after accounting for the size distribution scalings and using the same assumptions as in P1, i.e. an albedo

[4]More subtly, surveys at different latitudes and longitudes probe different average distances as they look into the trans-neptunian region due to the different distance distibutions of resonant and non-resonanat populations; thus a given apparent magnitude depth actually probes at different average size limit. Stating a population limit to a stated H-magnitude limit is thus more meaningful.

of p_g=0.05, hence $H_g(D_p$=100 km) = 9.16. Hahn & Malhotra (2005) give an essentially-identical estimate of 130,000 TNOs with $40.1 < a < 47.2$ AU and $D > 100$ km (with no error estimate), which is certainly within our 95% confidence region even with the small differences in albedo and phase-space boundaries used. If we use constant α values for the two components and extrapolate to $D >$100 km, we find the same population estimate as Hahn & Malhotra (2005) and are a factor of a few higher than Trujillo et al. (2001) (see Appendix C).

Our current estimates agree with P1 when scaled to the $H_g < 8$ limit where CFEPS is sensitive. Thus, it appears that the main belt's population for $H_g < 8$ is secure, where we have provided the first detailed breakdown of the hot and cold component's individual populations and detailed sub-structure.

5.1.4. Discussion

Some characteristics of the main classical belt that require explanation are the bimodal nature of the inclination distribution, the relative importance of the so-called hot component, and the marked sub-structures in (a, e) space for the low-inclination objects.

Jewitt et al. (1998), Trujillo et al. (2001), Allen et al. (2001), Trujillo & Brown (2001) and Kavelaars et al. (2008), reported the existence of an edge of the Kuiper Belt at 47–50 AU. Because the samples on which they based their estimate were heavily biased towards low-inclination objects, they were really detecting an edge of the cold component of the classical belt. In addition, Figure 14 of Trujillo et al. (2001), Figures 2 and 3 of Trujillo & Brown (2001), and Figure 3 of Kavelaars et al. (2008) all show a marked peak at around 44 AU followed by a very fast decrease in the number of objects past 44.5–45 AU, with perhaps a low density tail past 50 AU. The above papers vary in how sharp they consider the "cut off" to be. In hindsight it is clear that what they were reporting as an edge is in fact due the presence of the low-inclination kernel and stirred components, which dominate the low-latitude detections and fall off quickly beyond 45 AU. As Kavelaars et al. (2008) point-out, the peaked nature of the distribution is absent in the 'hot' component and entirely absent from the 'scattering disk' population. The stirred component's density is a rapidly-decreasing function of semimajor axis that becomes very small by the time the 2:1 resonance is reached. This hints at a possible connection between the kernel, the stirred component and the migration of the 2:1 to its current location; this outer edge appears only in the low-inclination component. We will show below that a scenario with the hot component continuous across the 2:1 resonance is in agreement with the data.

The L7 sample contains a cluster of 6 objects with large e and i just interior to the 2:1 MMR. Amongst these, only the one with $a < 47$ AU (L4k17, $a = 46.967$) was included in our analysis of models of the classical belt, the other five being in the region where the exact limit of the resonance is not easy to analytically define. This cluster could very well be a group of objects "dropped out" when the 2:1 MMR shrank at the end of Neptune's evolution (Sec. 7).

Gulbis et al. (2006) reported a difference between the B-R color of the 'Core' and the 'Halo', the former being redder than the latter, from photometric measurement they later acquired on the DES sample.

Table 5. Model dependent population estimates.

	$N(\mathrm{H}_g \leq 8)$	$N(\mathrm{D} \geq 100\mathrm{km})$
Inner Classical Belt		
All	400^{+400}_{-200}	$3,000^{+3,500}_{-2,000}$
Main Classical Belt		
Hot	$4,100^{+900}_{-800}$	$35,000^{+8,000}_{-7,000}$
Stirred	$3,000^{+700}_{-600}$	$75,000^{+17,000}_{-15,000}$
Kernel	900^{+200}_{-200}	$20,000^{+5,000}_{-5,000}$
All	$8,000^{+2,000}_{-2,000}$	$130,000^{+30,000}_{-27,000}$
Outer/Detached Classical Belt		
All (a >48)	$10,000^{+7,000}_{-5,000}$	$80,000^{+60,000}_{-40,000}$

Note. — Our model estimates are given for each sub-population within the Kuiper belt. The uncertainties reflect 95% confidence intervals for the model-dependent population estimate. Values for N(D>100 km) are derived assuming an albedo of p_g=0.05, hence $H_g = 9.16$. Remember that the relative importance of each population will vary with the upper H_g limit.

Our orbital survey was also not designed to yield precision photometry, and the $g-i$ and $g-r$ colors that we can obtain from Table 7 are too uncertain to address this point.

In Sec. 8 we discuss some consmogonic implications of these features, review how well the current models reproduce them, and propose future directions.

5.2. The inner classical belt

The 'inner' classical belt is the non-resonant and non-scattering population between Neptune and the 3:2 resonance. Paper P1 contained only two such TNOs, preventing us from deducing a detailed description of this region of the Kuiper belt. There are six inner classical belt objects in the L7 sample (see Table 3), providing the opportunity to start constraining an orbital distribution. The phase space is cut by the ν_8 secular resonance which eliminates almost all inner-belt TNOs with $7^\circ < i < 20^\circ$ making the intrinsic inclination distribution difficult to interpret. If one uses a definition of 'cold' belt as those objects with $i < 5^\circ$ (*eg., Lykawka & Mukai 2007)*, one concludes that a large fraction of the inner belt is cold. Such an analysis, however, neglects the bias towards detecting the lowest-i TNOs from the hot population in ecliptic surveys and the removal of moderate inclination objects via the ν_8. Determining the intrinsic orbital distribution of the inner belt is precisely the sort of problem in which a simulator approach provides a clearer understanding.

5.2.1. Parametric Model

For the inner-belt population we utilized the same form of semi-major axis and perihelion distance distributions as for the hot component of the main classical belt (see Appendix A), changing the range of semi-major axis to be $37 < a < 39$ AU and fixing the size distributions for the hot and cold components to be the same as those found for the main belt populations. We then attempted to find a model that included both a hot and a cold component using the same inclination widths and fractions as for the main belt, these models were rejected at >95% confidence. Using the same (a, q) model but with a single-component inclination distribution width of $\sigma_h = 16^\circ$, like the main belt's hot component (cutting away $7^\circ < i < 20^\circ$ orbits as they were proposed) provides a perfectly-acceptable match to the L7 inner-belt detections. In fact, inclination widths of $5^\circ < \sigma_h < 20.0^\circ$ were found to be acceptable. Even restricting one's attention only to the inner-belt TNOs with $i < 7^\circ$ (inclinations below ν_8 instability region) still requires an inclination distribution wider than the cold component of the main belt, indicating that the evidence against an inner-belt cold component comes from not just the largest-i detections.

5.2.2. *Population Estimates*

Using a single component model with $\sigma_h = 16^\circ$ and $\alpha = 0.8$ we determine $N_{\rm inner}(\mathrm{H}_g \leq 8.0) = 400^{+400}_{-200}$ (Table 5). This estimate is in good agreement with the L3-sample's estimate of 290^{+690}_{-250}. As before, the uncertainties reflect 95% confidence limits given the intrinsic model distribution and does not reflect our uncertainty in the model. These random uncertainties are a factor of two, due to the small number of inner belt detection.

5.2.3. *Discussion*

Romanishin et al. (2010) compared photometric colors of inner-belt TNOs to other categories and found a good match between the inner belt and the high-inclination objects from the main belt, while a marked difference from the low inclination objects from the main belt, supporting the "hot-only" hypothesis. To attempt to duplicate the conclusion, we compared our photometric data for each population. Unfortunately, but also unsurprisingly, the quality of our photometric data is insufficient for such a comparison. The median uncertainty on our $g-i$ and $g-r$ colors is ~ 0.25, which is about five times more than for the Romanishin et al. (2010) data. We are thus unable to provide additional verification from our current photometric colors.

The successful use of the same orbital distribution for the inner belt and the main-belt's hot component suggests that the entire inner belt may be the low-a tail of the hot main belt. This would be a cosmogonically appealing unification of the sub-populations of the Kuiper Belt. If true, then (at least to order of magnitude) the TNO linear number density at the boundary (we chose 40 AU) extracted from each model should be comparable. Denoting $P(\mathrm{H}_g < 8.0)$ as the number of objects per AU with $\mathrm{H}_g < 8.0$, we find $P_{\rm inner}(\mathrm{H}_g < 8.0, 40\ \mathrm{AU}) = 270^{+180}_{-100}\,\mathrm{AU}^{-1}$. For the hot main belt, $P_{\rm main}(\mathrm{H}_g < 8.0, 40\ \mathrm{AU}) = 670^{+160}_{-140}\,\mathrm{AU}^{-1}$. At this interface, the hot main-belt number density is ~ 3 times that of the extrapolated inner belt. Given the very uncertain nature of these estimates and the fact that they are anywhere close leads us to postulate that the inner-belt and hot-main TNOs were emplaced by a single cosmogonic process. In this hypothesis, the reduced inner-belt density would be due to the smaller volume of stable phase space in the inner belt region (because there is a smaller available stable range of e) as well as the significant range of inclinations from 7° to 20° destablized by the ν_8 . Scaling the inner-belt population density, to account for this reduced inclination range, results in $P_{\rm inner}(\mathrm{H}_g \leq 8.0, 40\ \mathrm{AU}) = 500^{+300}_{-200}\,\mathrm{AU}^{-1}$, consistent with the value from the main belt estimate at the 2σ level. Figure 8 presents the linear number density versus a for the scaled inner belt[5] compared to those of hot main belt and outer+detached populations.

In this picture, the lack of a cold inner-belt component is significant. Assuming that the cold component originally existed in this region, the plausible mechanism for the cold component's destruction is the ν_8 resonance sweeping out through the inner belt at some time, eliminating all low-i TNOs. The nearby 3:2 mean-motion resonance also lacks a cold component (Brown 2001; Kavelaars et al. 2008), which argues

[5]The 7-20° portion of a $\sin i \exp(-0.5 i^2/(16^{\circ 2})$ inclination distribution accounts for 46% of the $\sin i$-weighted phase space; to correct a population in the remaining phase space back to the original needs to be multiplied by 1/(1-0.46) = 1.85.

that if it swept slowly through the 36–39 AU region the cold component must have already been removed; otherwise, Hahn & Malhotra (2005) show that the low-i objects should have been captured into the 3:2 and preserved (because the 3:2 shields its members from the effects of the ν_8). One possible interpretation is that the 3:2 only obtained particles from a scattering hot population (as in the Levison et al. (2008) model) and ended with a large jump to its current location, but a reason for the lack of a cold population inside 39 AU would need to be provided. Because the 3:2 location depends on only the semimajor axis of Neptune, one might expect that the 3:2 resonance's arrival at its current value would occur before the ν_8 reaches its current location due to the latter's dependence on the orbital elements of multiple planets and the existence of other remaining mass in the system (Nagasawa & Ida 2000).

5.3. The outer edge of the hot belt

We successfully construct a model of the non-resonant, non-scattering TNOs with semimajor axis beyond the 2:1 resonance by simply extending the L7 main-belt model out into this region. Using the classification system from Gladman et al. (2008), our current sample contains 3 outer-belt TNOs and 11 detached TNOs; the distinction between them is set by an arbitrary cut in eccentricity at $e = 0.24$. For our current analysis, we group these two populations, under the hypothesis that they share a smoothly-varying orbital distribution.[6]. In order to avoid problems with the exact border of the 2:1, we start our modelling at $a = 48$ AU; this eliminated 1 detached TNO, reducing our sample to 13.

The outer/detached objects share the same (q, i) distributions as the hot main classical belt. This suggests that again (as for the inner belt) the outer population may be a smooth extension of the main-belt hot component. To model the outer/detached TNOs, we thus use the same prescription as for the hot-main classical belt, with $\alpha = 0.8$ and an a range from 48 AU to a value $a_{\max}$, with density varying as $a^{-\beta}$, with $\beta = 2.5$. We tried varying the exponent β of the a distribution. For shallow distributions, i.e. $\beta \leq 1.5$, the model is rejected when $a_{\max}$ exceeds ∼100 AU, because it creates too many simulated detections close to $a_{\max}$. The range $2.0 \leq \beta \leq 3.0$ produces acceptable models with no constraint on $a_{\max}$. Models with larger values of β exhibit a very steep decrease of number density at large a and fail to produce enough detections with a >60 AU. We thus adopt $\beta = 2.5$, as for the main classical belt. The number of objects needed to reproduce our 13 outer/detached detections is insensitive to our choice of $a_{\max}$ due to the strong detection biases. Hence we formulate our population estimate for a population with no outer edge, finding a population beyond 48 AU of $N_{\rm outer/detached}(\mathrm{H}_g \leq 8.0) = 10,000^{+7,000}_{-5,000}$ (see Table 5). Of these, only a small number $N_{\rm outer}(\mathrm{H}_g \leq 8.0) = 500^{+350}_{-250}$ have $e < 0.24$, thus belonging to the outer belt defined by Gladman et al. (2008).

As for our analysis of the inner belt, we computed the number density of TNOs per unit a at a main/outer interface at 47 AU, $P_{\rm outer/detached}(\mathrm{H}_g \leq 8.0, 47\ \mathrm{AU}) = 340^{+230}_{-150}\,\mathrm{AU}^{-1}$ and compare it to

[6]Although it remains to be seen if the very large-inclination objects like Buffy (Allen et al. 2006) or Drac (Gladman et al. 2009) are part of such a distribution.

the value from the outer edge of the main belt $P_{\rm main,outer}(\rm H_g \leq 8.0) = 490^{+110}_{-100}\,AU^{-1}$. Hence the TNO number density per unit a in the outer/detached belt is the same as that of the hot main belt, within uncertainties. There was absolutely no coupling in the debiasing procedure of these two TNO populations; this matching result was not tuned in any way. Figure 8 demonstrates that an initially-uniform semimajor axis distribution for all three of these Kuiper belt sub-components as a single dynamical population is a plausible scenario.

Given the number of papers discussing a noticable edge to the distribution (Jewitt et al. 1998; Allen et al. 2001; Trujillo & Brown 2001) this continuity may be surprising. Realize that the continuity is in the hot component, which our analysis indicates is actually present throughout the region from Neptune to at least several hundred AU. This population has a pericenter distribution with very few q's above 40 AU, and may very well have been emplaced as a sort of *fossilized scattered disk* (Gladman et al. 2002) as illustrated in Morbidelli & Levison (2004). This same process, however, does not emplace the kernel and stirred components which dominate the main-belt region for $H_g > 8.0$, nor produce the dramatic fall-off beyond 45 AU in these cold populations.

6. The scattering disk

If the Centaurs and then JFCs do indeed come from one of the Kuiper Belt's sub-populations, then their penultimate meta-stable source will be the set of TNOs currently scattering off Neptune, as defined by Morbidelli et al. (2004) and Gladman et al. (2008). Hence we wish to give a population estimate for this 'actively scattering' population. Unfortunately the region occupied by the scattering objects is not a simply-connected region definable by a simple parameter-space cut; they are intimately mixed with stable resonant and non-resonant objects and providing a full dynamical model of this region is well beyond the scope of the current manuscript. Here we examine available models of the scattering disk using the CFEPS Survey Simulator to provide an order of magnitude population estimate for this important transient population.

The definition of the *scattering* population has evolved over the last 15 years. A cosmogonic perspective is easily adopted by workers doing numerical simulations. In such simulations the 'scattered' disk is taken to be comprised of TNOs that currently do not have encounters with Neptune but were delivered onto those orbits via an encounter. Morbidelli et al. (2004) quantified this definition by requiring that scattered TNO needs to have it semi-major axis change by more than 1.5 AU over the life of the Solar System. In this process, knowledge of orbital history is required for classification and, clearly, this information is not available for a given real TNO. More problematically, if the Levison et al. (2008) model is correct then the entire Kuiper Belt would qualify as having scattered off Neptune, making the term *scattered disk object* a meaningless distinction. Gladman et al. (2008) proposed a practical definition for classification based on the orbit of known objects at the current epoch, in which the 'scattering objects' are those *currently* (in the next 10 Myr) undergoing scattering encounters with Neptune in a forward simulation. In the current manuscript we consider two definitions of the scattering disk, one based on a parameterized region of phase space and one based on numerical modelling of a particular scattering process, to derive an estimate of the scattering

population.

Trujillo et al. (2000) and Hahn & Malhotra (2005) both give population estimates of the scattered Kuiper Belt, but based on different definitions of this population. The former called the scattered Kuiper Belt the region of phase space $50\ \mathrm{AU} \leq a \leq 200\ \mathrm{AU}$ and $34\ \mathrm{AU} \leq q \leq 36\ \mathrm{AU}$. Based on their detection of 4 objects with preliminary orbits in this region, they provide a population estimate of 18,000–50,000 objects (1-σ range) with $D > 100$ km, assuming an H_g distribution slope of 0.8. Using CFEPS and the same orbit and H_g distributions as Trujillo et al. (2000) we estimate the population in that region of the phase space to be 2,100–17,500 objects (95% confidence range), about a factor of 4 less than Trujillo et al. (2000)'s estimate. This estimate is based on scaling the Survey Simulator's detections to match all the L7 detections in this range of q. Awkwardly, *none* of the L7 detections with orbits in this q range are actually members of the scattering class, thus this estimate is more correctly an estimate of some restricted portion of the Detached population. Two of the objects (1999 CV_{118} and 1999 CF_{119}) used by Trujillo et al. (2000) for their population estimate were later found to not have orbits in the region they termed the scattered disk, hence their population estimate of this region should be divided by 2, making it more compatible with our estimate[7]. The choice of the q=34–36 AU region was motivated by the candidate 'scattering' orbits known to Trujillo et al. (2000), intending this to be a source region for the Centaurs and JFCs, as postulated by Duncan & Levison (1997). However, the majority of the known TNOs in that phase space cut are not currently interacting with Neptune and are on resonant or detached orbits (Gladman et al. 2008). A simple phase-space cut is not appropriate for the scattering disk population.

To obtain an order-of-magnitude population estimate via a dynamical model, we used the result of numerical integrations by Gladman & Chan (2006). This model attempted to produce the detached population via secular interaction with rogue planets, where the additional planet persists for the first 200 Myr of the simulation. Gladman & Chan (2006) find that the scattering particles in their simulations that survive to the end of the a 4 Gyr integration largely forget their initial state. To obtain a scattering disk model, we selected the orbital elements of actively scattering test particles during the last 500 Myr of one 4.5-Gyr integration. We then slightly smeared the orbital elements and applied an H-magnitude distribution with slope α=0.8. We found a reasonable match between the orbital elements of the L7 scattering sub-population and our input scattering model, as observed by the Survey Simulator, althought the inclination distribution was somewhat too cold, yielding a confidence level of only 8%. The apparent magnitude distribution was rejected at more than 99% whatever the slope of the H_g distribution we used; it is plausible that this rejection is due to a change in luminosity-function slope in the size range probed by our observations, as the faintest absolute magnitude of our detections is $H_g = 10$ because scattering TNOs include many $q < 30$ AU members. Three of the CFEPS active scatterers were inside 30 AU at the time of detection. The match between the orbital model and the observations allow us to be reasonably confident our population estimate is good to a factor of ten and we do not feel this order of magnitude estimate warrants further tuning until a larger sample of scattering objects is in hand. While there is clearly future room to better test models, we give here the first published estimate of the active scattering population. The results are given in Table 6 for $H_g < 10$ and for

[7]The other two sources (1999 TL_{66} and 1999 CY_{118}) are found to be on scattering obits (Gladman et al. 2008).

diameter D >100 km ($H_g < 9.16$ assuming an albedo of p_g=0.05). The quoted factor-of-three uncertainty accounts only for the Poisson variation.

We estimate an actively-scattering population that is about 2-3% that of the sum of the classical belts. Interpretation of this number is problematic. A very large actively-scattering population would require that the current disk could not be the steady state intermediary between the Centaurs and a longer-lived source in the trans-neptunian region, in which case the currently actively-scattering population is more likely to be the long-lived tail of a roughly 100× more populous primordial population (Duncan & Levison 1997). For the 2-3% figure, the active scatterers could conceivably be now dominated by objects that have left the resonant, detached, or classical populations in the last Gyr.

7. Testing cosmogonic Kuiper belt models

The CFEPS-L7 model is an empirical parametric model that properly reproduces the observed orbital distribution of the Kuiper belt, once passed through our survey simulator. The purpose of this parametric model is to provide absolutely-calibrated population estimates of the various sub-populations of the Kuiper belt. The model also exhibits important features of the intrinsic Kuiper belt that a cosmogonic model should reproduce. For example, one needs to produce a cluster of objects at low inclination and low eccentricity near 44 AU, that we call the kernel. There is also a low-i component extending from the outer edge of the ν_8 secular resonance at 42.4 AU out to the 2:1 MMR with Neptune. Finally, there is a hot component with a confined q range that extends in semimajor-axis from the inner belt at ∼35 AU out to several hundred AU with a decreasing surface density. The synthetic L7 model is also useful for observational modeling of our Kuiper belt, with Stark & Kuchner (2010) as an example for the outer Solar System dust distribution based on the L3 model.

The ability to provide a detailed quantitive comparison with a cosmogonic model is, however, the true power of the CFEPS survey. This is done by passing a proposed model of the current Kuiper Belt distribution through the CFEPS survey simulator and then comparing this detection-biased model with the real CFEPS detections. Through this procedure one can choose between models in a statistically robust way. Both the CFEPS L7 synthetic model and the CFEPS survey simulator are available from the project web site *www.cfeps.net*.

Several models have been proposed to explain the dynamical structure of the Kuiper belt (Malhotra 1993; Ida et al. 2000; Hahn & Malhotra 2005; Levison et al. 2008, to name a few). Since the primary

Table 6. Scattering disk population estimates.

	$N(\mathrm{H}_g \leq 10)$	$N(\mathrm{D} > 100\mathrm{km})$
Scattering disk	$25,000^{+20,000}_{-15,000}$	$5,000^{+5,000}_{-3,000}$

purpose of CFEPS was to validate or refute cosmogonic models, we present an example of this process. Because we had available both an orbital element distribution and a resonance-occupation analysis (Levison, 2010, private communication), we have chosen to use Run B of Levison et al. (2008) as an example of how one uses the CFEPS Survey Simulator to compare a model to the observed Kuiper belt. The simulation in question (motivated by the Nice model of the re-arrangment of the outer Solar System) has already some known problems pointed out by its authors, but the model's intriguing aspects make it a good example of the comparison process.

All the fictitious TNOs in the Run B model were dynamically classified following the Gladman et al. (2008) procedure (Van Laerhoven, 2010, private communication). The final planetary configuration in the Nice model was intentionally made different from that of the Solar System to avoid the ν_8 secular resonance inadvertently sweeping through and destroying the belt and thus has many objects in the $40 < a < 42.4$ AU range at low inclination, where the real ν_8 resonance would eliminate them. To avoid this complication, we restricted the comparison to the range $42.4 < a < 47$ AU, yielding 128 non-resonant model TNOs from run B.

We use the following procedure to generate the large number of TNOs required as input to the survey simulator. First we select a model object at random, and vary the orbital elements uniformly by ± 0.2 AU in both a and q and $\pm 0.5^\circ$ in inclination and then randomize the elements Ω, ω, and M, There was no size distribution given for the model objects, so the H_g magnitude of each object was drawn from an exponential distribution (eq. 5.1.1). Given the orbital elements and H_g magnitude, we then use our Survey Simulator to determine if the model object would have been detected by the CFEPS-L7 obersvations. We repeat the procedure until we have a set number of simulated detections and then compare the a, e, i, q and r one-dimensional cumulative distributions of the simulated detections to those of the L7 sample, using the Anderson-Darling test.

For the H_g distribution, we tried single slopes of $0.6 \leq \alpha \leq 1.3$ and also a model with $\alpha = 1.2$ for the low-i and $\alpha = 0.8$ for the high-inclination objects, as in our favored model. All the models for the H_g distribution produced acceptable matches to the apparent magnitude distribution, but had no effect on the orbital element distributions, so we do not show the magnitude distribution.

Fig. 9 compares the distribution of a, e, i and r of the L7 sample and simulated detections from the model. There is remarkably-good agreement for the a distribution. Although the Nice model does not exhibit a clustering around 44 AU as strong as the L7 sample, the difference between the two distribution is not statistically significant.

On the other hand, the model's e distribution is too excited compared to the observed one, as already noted by Levison et al. (2008). This then results in detection distances that are overly dominated by small-distance detections. For both cumulative distributions, the Anderson-Darling test says that the hypothesis that the observed objects could be drawn from the model can be rejected at $>$99.9% confidence.

The model's i distribution is not a good match either, again as already noted by Levison et al. (2008); the AD test rejects the i distribution at more than 99.9% confidence. This is mostly because the L7 distribution has two components, while the Run B input model gives an essentially unimodal distribution. The simulated

detections from the model appear roughly consistent up to $i \simeq 4°$, but there is a lack of high-i TNOs, to which the Anderson-Darling test is sensitive. Run B lacks the hot component that peaks between 15° and 20° and extends past 30°. Looking only at the $i < 6°$ region, here too the AD test rejects the model at more than 99.9% confidence. Most of the Run B classical belt comes from the low-i outer part of the planetesimal disk, which acquires inclinations similar to that of the inner initial disk, with a width 6°. The true cold component, on the contrary, has a width certainly less than 3°. We conclude that one needs a strongly bi-modal input population to the Nice model in order to produce the desired bi-modal inclination distribution we see in the real Kuiper belt. More worrying is the claim by Levison et al. (2008) that increasing the width of the initial population produced the same final inclination distribution, meaning there is a missing ingredient in this model to explain the dynamical structure of the Kuiper belt. Levison et al. (2008) mention another simulation, Run E, which generated too many hot objects compared to the cold population; so there may be an intermediate parameter set that could match the observations.

8. Conclusions

This paper's modeling concerns the non-resonant Kuiper Belt, although the L7 release lists all detections from the CFEPS survey fields from 2002–2007 for the sake of completeness. Due to the complexity of the modelling required because of the phase relations with Neptune, the resonant populations are presented in a separate paper (Gladman et al. 2011). We find that the debiased orbital and H-magnitude distributions show that there is considerable sub-structure in the main Kuiper Belt. We quantitatively measured the size of the various sub-populations, create an empirical model of these sub-populations in the L7 synthetic model, and provide an algorithm (the CFEPS survey simulator) to quantitatively compare cosmogonic models to the intrinsic Kuiper Belt. Here we summarize the results and offer a synthesis and interpretation.

A plausible hypothesis is that the hot population permeates the entire Kuiper Belt region from 30 AU up to at least 200 AU, albeit with a projected surface density (onto the invariable plane) that decreases with semimajor axis. Even the resonant populations are consistent with the idea that the entire hot component is a vestigal "fossilized" scattered disk from an epoch when TNOs with perihelia up to ∼40 AU were being weakly scattered by a massive object at the inner edge of the Kuiper Belt (whether this object was Neptune or something else is unclear from the present data). The inclination distribution of this hot population can be represented by $\sin(i)$ times a gaussian of width $\sim 16°$. Note however that, due to the strong bias against detection of large-i objects in an ecliptic survey, our current sample does not provide a strong constraint on the width or the functional form of the hot component. A scenario in which the inner belt, hot main-belt, outer belt and detached populations, along with the resonant populations were all emplaced simultaneously from a population scattered outward during the final stages of planet formation, with a single size distribution, initial inclination distribution, colour distribution and binary fraction, is an attractive hypothesis. The plausibly-continuous initial number density across the inner/main and main/outer boundary (see Fig. 8) supports this idea.

The Kuiper Belt's (surviving) 'cold' population is entirely confined between semimajor axes of 42.4 AU

and the 2:1 resonance with Neptune, and its inclination distribution (measured relative to the J2000 ecliptic) is adequately represented via $\sin(i)$ times a gaussian of width 2.6°, with an acceptable range from 2.3° up to 3.5°. There are indeed $i < 5°$ TNOs in the low-i tail of the hot population all over the Kuiper belt and even in the $42.4 < a < 47$ AU region, so an inclination cut does not provide a clean separation between the hot and cold components of the main belt. In the current belt we claim that all $i < 5°$ TNOs with semi-major axis outside the above range are the hot-component objects that happen to have lower inclinations. The cold population exhibits a particularly-strong grouping in band of about 1-AU a thickness, centered at 44 AU (which we call the kernel). The linear number density (#/AU) of 'cold' belt objects increases from the inner edge at 42.4 AU up to a maximum at ~ 44.4 AU, all with rather low eccentricities. Past 44.4 AU, the linear number density drops noticeably, and classical TNOs tend to have higher eccentricities; the CFEPS-L7 model uses a 'stirred' population that covers the 42.4–47 AU range with a single parameterization. We favor the idea that this cold component is primordial (the objects formed at roughly their current heliocentric distances), although this is not required.

The primordial distance range of the cold population is difficult to constrain. The inner boundary at a=42.4 AU may have been eroded via scattering by massive bodies and resonance migration; an important condition is that any sequence of events cannot allow either the inner belt, or the mean-motion and secular resonances that probably migrated through it, to have preserved a cold component today. The coincidence of the stirred population's outer edge with the 2:1 resonance suggests to us that the kernel marks the original outer edge and that the larger-a cold objects have either (i) been dragged out of the $a < 44.4$ AU region via trapping and then drop-off in the 2:1 as it went past (in the fashion studied by Hahn & Malhotra (2005)) or (ii) due to weak scattering out of the $40 < a < 44.4$ AU region. Perhaps the edge of the original cold population around 45 AU may be explained by the global evolution of solid matter in turbulent protoplanetary disks (Stepinski & Valageas 1996, 1997), although an even-more extreme density contrast may be needed at ∼30 AU to prevent Neptune's continued migration outward (Gomes et al. 2004). Sharp drops in surface density are commonly observed in protoplanetary disks at about this 30–50 AU scale (Johnstone et al. 1998; Mann & Williams 2009, 2010).

There is an issue with a primordial origin of the cold population at this location. The on-ecliptic mass density of this population is extremely low and it would be difficult to form multi-hundred km TNOs in a low surface density environment. This may not be impossible due to recent work on forming planetesimals big (Morbidelli et al. 2009a; Youdin 2011), which can be favored by external photoevaporation (Throop & Bally 2005), and may be supported by the fact that it appears that there are simply no cold objects larger than $H \sim 5$; all the larger objects are in the other populations which may come from closer to the Sun where the mass density was higher.

The kernel around 44 AU is an intriguing feature. A collisional family explanation would eliminate the idea that the 44.4-AU edge is a primordial edge, but would instead simply be where the very-low velocity dispersion breakup occured. This velocity dispersion is even lower than for the putative Haumea collisional family (Brown et al. 2007). An additional puzzle is the unclear significance that the kernel is bounded between the 7:4 and the 9:5 MMRs . One possible, very ad-hoc, explanation would be that the 2:1 MMR started its migration interior to 43.5 AU while being wide (due to a large Neptune eccentricity), and then

had a stochastic jump by a few tenth of AU while near 44 AU, leaving behind a pile of objects that we see as the kernel today.

The hot population poses other strong constraints. Models by Gomes (2003); Hahn & Malhotra (2005); Levison et al. (2008) all succeed in creating a hot population that has a similar radial extent to what is currently observed, but have varying success in matching the inclination distribution. When slowly migrating Neptune over long distances (> 8 AU) into an initially-cold disk, Gomes (2003) and Hahn & Malhotra (2005) generated a reasonable TNO fraction with inclinations up to 35°. When migrating Neptune over a shorter distance (Gomes 2003), or in a hot disk (Hahn & Malhotra 2005), the fraction of high-i TNOs is noticeably reduced, while still reaching the same maximum i. Levison et al. (2008), on the contrary, migrate Neptune over a short distance (2–3 AU) into a warm scattered disk (with $\langle i \rangle = 6°$) and essentially maintain the input inclination distribution. They report that increasing the initial i distribution resulted in the same final population, which lacks TNOs with $i > 30°$ and which we have confirmed is colder than the actual belt. These facts appear to indicates that Neptune had to slowly migrate over a long distance in a cold disk in order to obtain the observed inclination distribution of the hot population. However, Morbidelli et al. (2009b) showed that a long and slow migration of Neptune, coupled with a similar migration of the other giant planets, does not correctly reproduce the secular architecture of the solar system, in particular the amplitudes of the eigenmodes characterising the current secular evolution of the eccentricities of Jupiter and Saturn. They conclude that only the Nice model can reproduce the current dynamics of the inner solar system and the giant planets. Unfortunately this scenario does not produce Kuiper-Belt components with orbital properties that agree with the L7 orbit catalog.

The idea that the hot population originated from a planetesimal population scattered outward by Neptune, whose resonant and largest-q members are preserved, is extremely attractive. Thus much of Levison et al. (2008)'s general scenario has many pleasing aspects and one is tempted to think of the hot population as the transplanted population, even if our results show that the inclination distribution is a stumbling block. Contrary to some statements (eg Fraser et al. 2010), we find that the Nice model is not good at producing the the hot population's inclination distribution, but suprisingly produces rather well the cold population's fine structure in the semimajor axis distribution. The large-i TNOs which do appear could instead be interpreted as coming from the 'evader' mechanism of Gomes (2003). In this conception the Fraser et al. (2010) finding, that the luminosity distribution of the Jovian Trojans is more similar to the cold than hot TNO populations, makes perfect sense in a scenario in which the injection of bodies into the Jovian Trojan region occurs from the same source region as the implantation of the Kuiper Belt's cold population. In the Nice model this seems unlikely because jovian Trojan capture occurs just after the Jupiter-Saturn mutual 1:2 resonance crossing (Morbidelli et al. 2005) and involves small bodies closer to the planets than the cold outer disk that is the main source of the cold Kuiper belt. If so, the hot component cannot be generated from the Nice model's inclined inner disk, as this would have the same size distribution as the Jovian Trojans. One needs another source for the hot population, one that is not too perturbed by the initial instability in Neptune's motion. A final caveat concerns the existence of wide binaries in the cold belt; Parker & Kavelaars (2010) showed that the Neptune scattering occuring in the Nice model would disrupt nearly all such wide binaries, thus requiring a more gentle mechanism to move the cold-belt to its current location if that population did

not form *in-situ*.

Our current understanding of the trans-neptunian region is not likely to advance rapidly for time scales of order a decade unless new surveys begin to efficiently probe TNOs that were rare in the ecliptic surveys. The most likely approach that would result in an advance are moderate-depth (24th magnitude) wide-field surveys (many hundreds of square degrees) at higher ecliptic latitudes, or deeper (25th magnitude) surveys covering $\sim$ 100 sq. deg. targeting regions of sky that attempt to isolate cosmogonically-interesting sub-populations. We hope that CFEPS will serve as a standard for the need for well-characterized discovery and tracking. The Large Synoptic Survey Telescope (LSST) (Ivezic et al. 2008) should certainly firm up the main-belt dynamical sub-structure along with the colour and size distributions for those components.

A. Appendix A

In this Appendix, we give details of the algorithm used to generate the CFEPS-L7 model of the main classical belt.

The main classical belt objects are constrained in what is essential 3-dimensional phase-space due to the (confirmed a posteriori) fact that the mean anomaly and longitudes of ascending node and perihelion are all uniformly distributed in the intrinsic population. Thus the L7 model consists of 3 sub-populations constrained by 3 orbital-element distributions to determine for each sub-population.

The inclination distribution of each subcomponent is well represented by a probability distribution proportional to $\sin(i)$ times a gaussian $\exp[i^2/(2\sigma^2)]$, where past results indicate a 'cold'-component width of $\sim 2.5^\circ$ and a 'hot'-component width of $\sim 15^\circ$ (Brown 2001; Kavelaars et al. 2008).

The *hot* component occupies the semimajor axis range from 40.0 to 47.0 AU and is defined by:

- an a distribution with a Probability Density Function (PDF) proportional to $a^{-5/2}$, corresponding to a surface density proportional to $a^{-7/2}$;
- an inclination distribution proportional to $\sin(i) \times \exp[i^2/(2\sigma_h^2)]$, with width $\sigma_h = 16^\circ$;
- we eliminate objects from the region unstable due to the ν_8 secular resonance: $a < 42.4$ AU and $i < 12^\circ$;
- a perihelion distance q distribution that is mostly uniform between 35 and 40 AU, with soft shoulders at both ends extending over $\sim$1 AU; the PDF is proportional to $1/([1 + \exp((35 - q)/0.5)][1 + \exp((q - 40)/0.5)])$; any object with q <34 AU is rejected;
- finally, we reject objects with $q < 38 - 0.2i$ (deg) to account for weaker stability of low-q orbits at low inclination.

We have found that the exact form of the truncation at low perihelion distance is unimportant, as long as the

limiting value of q is a decreasing function of the inclination; this is justified dynamically as low-inclination orbits cannot have $q < 38$ AU and remain stable (Duncan et al. 1995).

The *stirred* component covers only the range of stable semimajor axis at low inclinations:

- an a distribution with PDF proportional to $a^{-5/2}$ between 42.4 (limit of the ν_8 resonance) and 47 AU;
- a uniform e distribution between 0.01 and a maximum value depending on the semimajor axis, $e_{max} = 0.04 + (a - 42) \times 0.032$, to reproduce the structure seen in figs. 2 and 3;
- randomly keep objects with probability $1/(1+\exp\left[(e - 0.6 + 19.2/a)/0.01\right])$, which corresponds to a soft cut at $q = 38 + 0.4 * (a - 47)$;
- an inclination distribution proportional to $\sin(i)$ times a gaussian of width $\sigma_c = 2.6°$;
- again, we reject objects with $q < 38 - 0.2 \times i$(deg) as for the hot component.

Finally, the *kernel* provides the group of objects with low inclination in the middle of the main classical belt as seen in fig. 2:

- a uniform a distribution between 43.8 and 44.4 AU;
- a uniform e distribution between 0.03 and 0.08;
- an inclination distribution proportional to $\sin(i)$ times a gaussian of width $\sigma_c = 2.6°$, identical to the stirred population.

For all components, the remaining orbital elements (longitude of node, argument of perihelion and mean anomaly) are drawn at random uniformly between 0° and 360°. All elements are generated in the invariable plane reference frame (inclination 1° 35' 13.86" with respect to J2000 ecliptic plane with direction of ascending node at 107° 36' 30.8"). In particular, we state widths of the inclination distribution with respect to the invariable plane. Elliot et al. (2005), Brown & Pan (2004) and Gulbis et al. (2010) studied the distribution of inclinations with respect to their self-determined Kuiper Belt Plane, which differ from the invariable plane.

To evaluate the acceptability of each model we evaluate our parameterization in distinct portions of phase-space.

- $i \geq 10$ deg
- $i < 10$ deg
- $a > 44.4$ AU
- $a \leq 44.4$ AU

- the entire main-belt region

We computed the probability of the AD or KKS statistics in each region separately and consider the minimum on all element distributions and all sub-regions when determining if a particular parameterization is rejected.

The variable parameters are the i-width of the hot component σ_h, the cold component's i width σ_c, the H-magnitude distribution of these two components (with slopes α_h, α_c), the hot population's fraction of the main belt f_h, and the kernel fraction f_k, with the stirred component forming the remainder: $f_s = 1 - f_h - f_k$.

The CFEPS-L7 model has the following known weaknesses:

1. Resonant orbits will be generated by chance in the main-belt region (especially for the 5:3, 7:4, and 9:5 resonances).

2. The ν_8 resonance cut is done in osculating, rather than proper, orbital elements space and thus some L7 model objects objects near the resonance will be unstable.

3. There are four tiny semimajor axis gaps in our model: small regions (~ 0.3 AU in a) on both sides of the 3:2 and 2:1 resonannces.

B. Appendix B

The CFEPS project is built on the observations acquired as the 'Very Wide' component of the CFHT Legacy Survey (CFHTLS-VW). All discovery imaging data is publicly available from the Canadian Astronomy Data Centre (CADC[8]). These images were acquired using the CFHT Queue Service Observing (QSO) system. For each field observed on a photometric night the CFHT QSO provides calibrated images using their ELIXIR processing software (Magnier & Cuillandre 2004). Our photometry below is reported in the Sloan system (Fukugita et al. 1996) with the calibrations contained in the header of each image as provided by ELIXIR. Color corrections were computed using the average color for Kuiper belt objects $(g - r) \sim 0.7$. Differential aperture photometry was determined for each of our detected objects observed on photometric nights and these fluxes are reported in Table 7. All CFEPS discovery observations were acquired in photometric conditions in a relatively narrow range of seeing conditions due to queue-mode acquisition. The photometry below supercedes information that may be in the Minor Planet Center's observational database.

[8]http://www.cadc.hia.nrc.gc.ca

Table 7. Object Fluxes.

Object	g	σ_g	N_g	r	σ_r	N_r	i	σ_i	N_i
L3f01	23.66	0.41	4	23.12	0.15	3	···	···	..
L3f04PD	22.74	0.33	4	···	···	..	···	···	..
L3h01	23.83	0.27	4	23.02	0.11	3	···	···	..
L3h04	24.32	0.17	4	23.82	0.33	7	···	···	..
L3h05	24.36	0.07	2	23.56	0.30	7	···	···	..
L3h08	···	···	..	23.15	0.75	7	···	···	..
L3h09	22.73	0.04	4	22.29	0.23	10	···	···	..
L3h11	23.44	0.20	7	23.13	0.10	3	···	···	..
L3h13	23.73	0.10	4	23.29	0.27	7	···	···	..
L3h14	23.27	0.15	3	22.81	1.42	8	···	···	..
L3h18	23.42	0.09	3	22.53	0.17	8	···	···	..
L3h19	···	···	..	23.67	0.26	9	···	···	..
L3h20	···	···	..	23.15	0.30	7	···	···	..
L3q01	23.89	0.21	3	22.96	0.17	3	22.76	0.36	3
L3q02PD	23.50	0.10	3	22.49	0.07	4	22.23	0.02	3
L3q03	23.19	0.17	4	22.36	0.25	4	22.37	0.00	1
L3q04PD	24.15	0.43	4	23.31	0.14	4	23.10	0.16	3
L3q06PD	23.58	0.30	4	···	···	..	···	···	..
L3q08PD	23.67	0.18	3	···	···	..	···	···	..
L3q09PD	23.50	0.24	4	···	···	..	···	···	..
L3s01	23.54	0.12	6	···	···	..	22.54	0.12	2
L3s02	23.81	0.28	6	23.40	0.23	4	23.18	0.11	2
L3s03	22.90	0.20	5	···	···	..	22.65	0.23	3
L3s05	23.67	0.30	5	···	···	..	22.88	0.13	2
L3s06	22.82	0.03	5	···	···	..	21.89	0.07	3
L3w01	22.89	0.61	5	···	···	..	···	···	..
L3w02	23.56	0.11	4	22.80	0.08	4	22.54	0.07	3
L3w03	23.76	0.07	5	22.50	0.08	4	···	···	..
L3w04	22.44	0.03	5	21.65	0.04	4	21.53	0.02	3
L3w05	24.20	0.31	4	23.70	0.17	3	23.77	0.07	3
L3w06	23.65	0.25	4	23.13	0.19	4	···	···	..
L3w07	22.95	0.09	5	···	···	..	22.46	0.09	3
L3w08	23.96	0.13	4	···	···	..	22.79	0.14	3
L3w09	23.53	0.10	3	22.72	0.15	4	···	···	..
L3w10	23.95	0.20	5	23.04	0.13	4	22.00	0.63	3
L3w11	24.03	0.12	4	23.49	0.15	4	23.34	0.13	3
L3y01	24.04	0.26	4	22.62	0.55	3	···	···	..
L3y02	23.38	0.09	6	22.69	0.19	4	···	···	..
L3y03	23.41	0.09	4	22.79	0.11	4	···	···	..
L3y05	23.89	0.03	4	22.99	0.12	3	···	···	..
L3y06	23.37	0.18	3	···	···	..	···	···	..
L3y07	23.42	0.09	4	22.87	0.23	5	···	···	..
L3y09	23.65	0.17	4	23.01	0.14	5	···	···	..
L3y11	23.82	0.32	4	23.51	0.21	4	···	···	..
L3y12PD	21.73	0.03	4	20.81	0.04	4	···	···	..

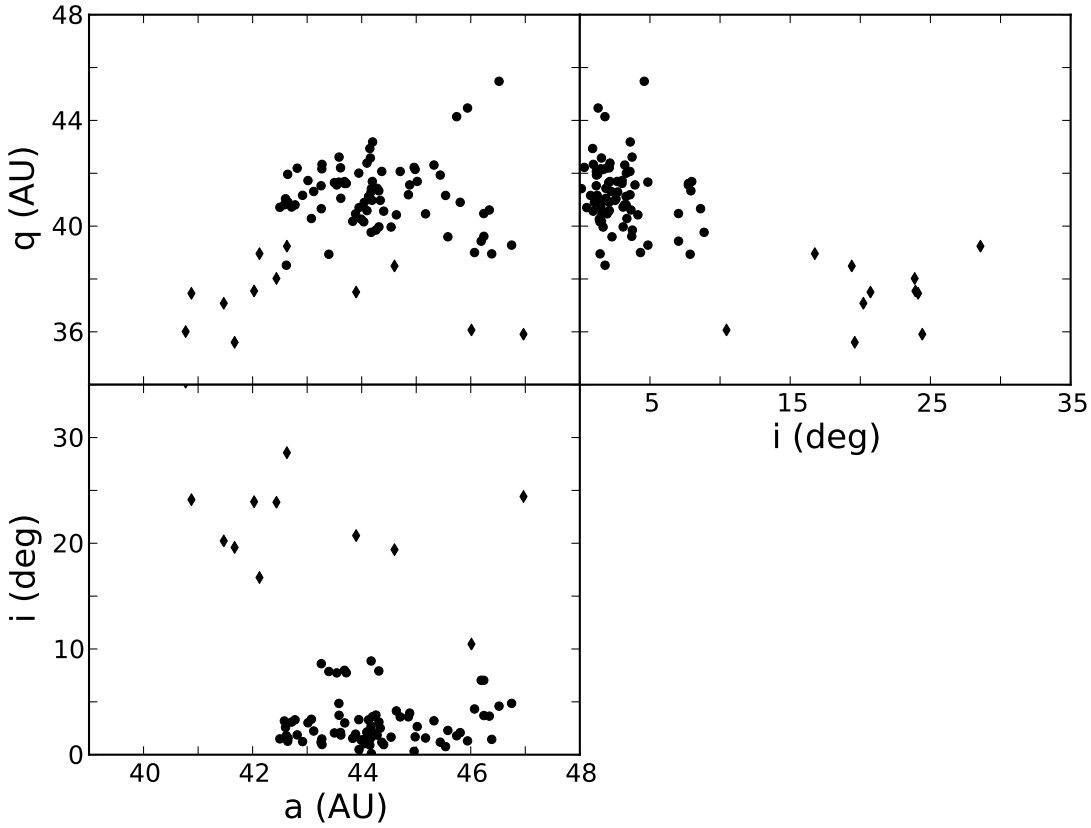
48
44
40
36
q (AU)
5
15
25
35
i (deg)
30
20
10
0
i (deg)
40
42
44
46
48
a (AU)

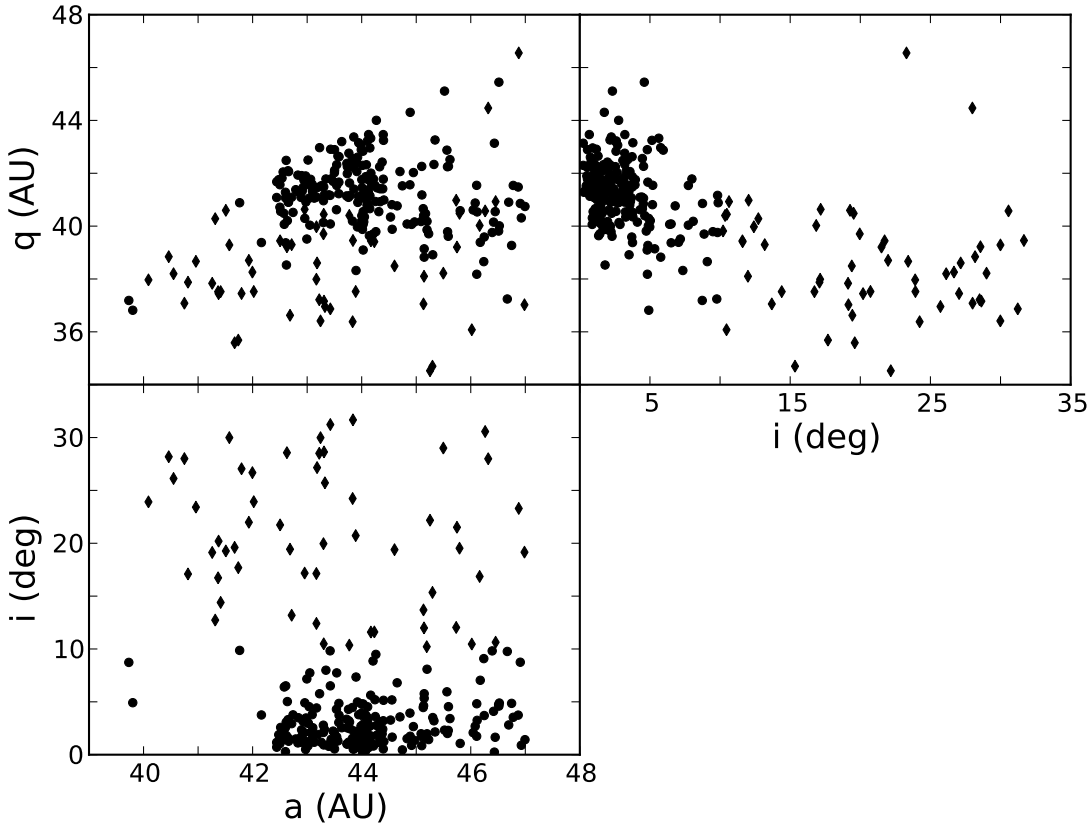
48
44
40
36
q (AU)
5
15
25
35
i (deg)
30
20
10
0
i (deg)
40
42
44
46
48
a (AU)

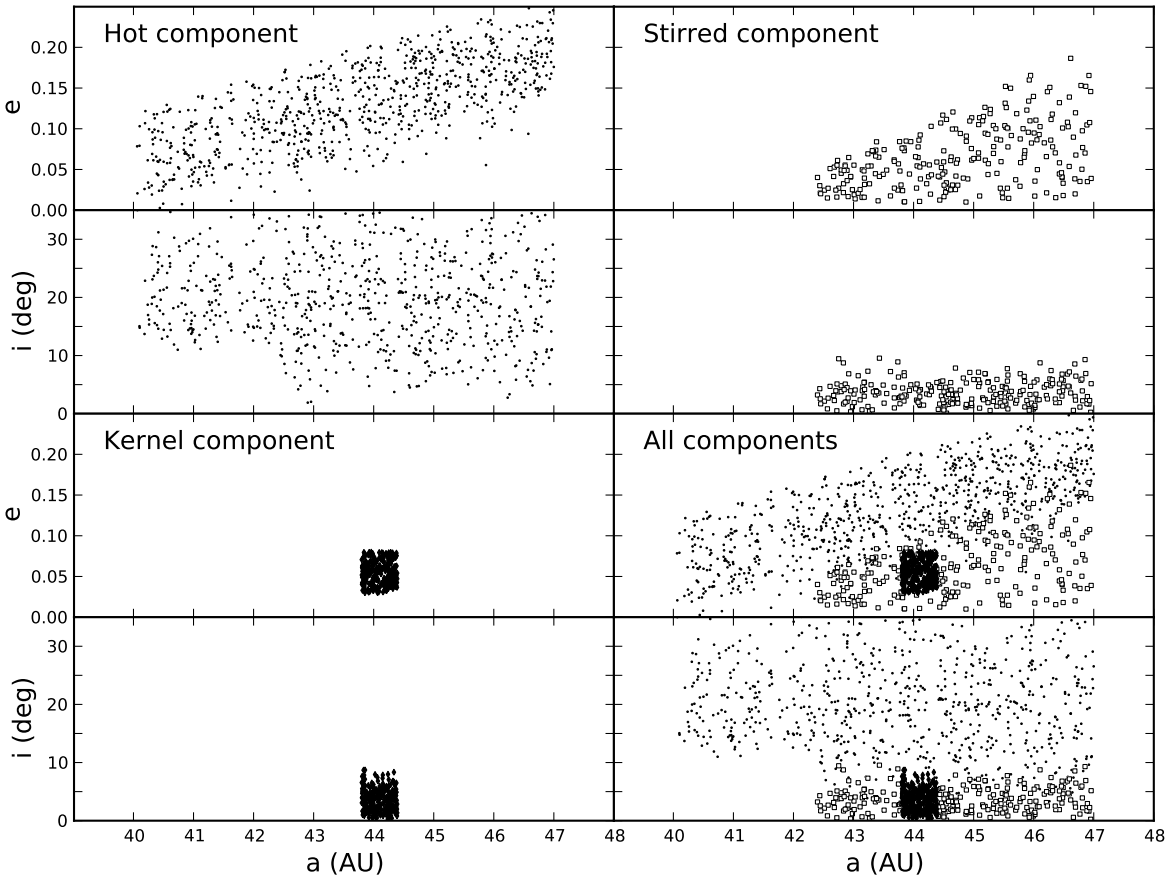
Hot component
Stirred component
Kernel component
All components
e
i (deg)
a (AU)
0.00
0.05
0.10
0.15
0.20
0
10
20
30
40
41
42
43
44
45
46
47
48

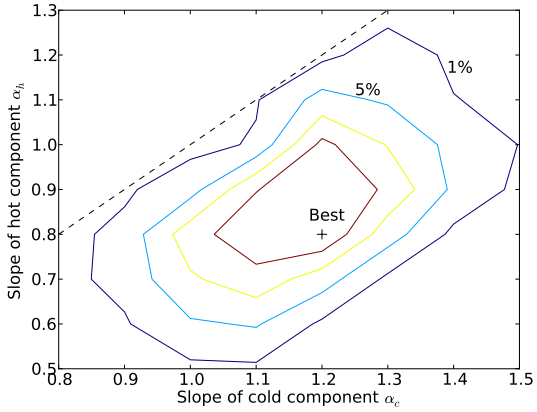

Fig. 5.— Contour plots of the 'minimum probability' statistic for a range of main classical belt models. Each model has a different slope of the H distribution for both the hot component (α_h) and the other components (α_c). Contour levels for 1% and 5% probabilities are shown. Acceptable models are interior to the 5% level curve. The dashed line indicates the locus with identical slopes for all components. Th e plus sign indicates the adopted model (which gave the best match).

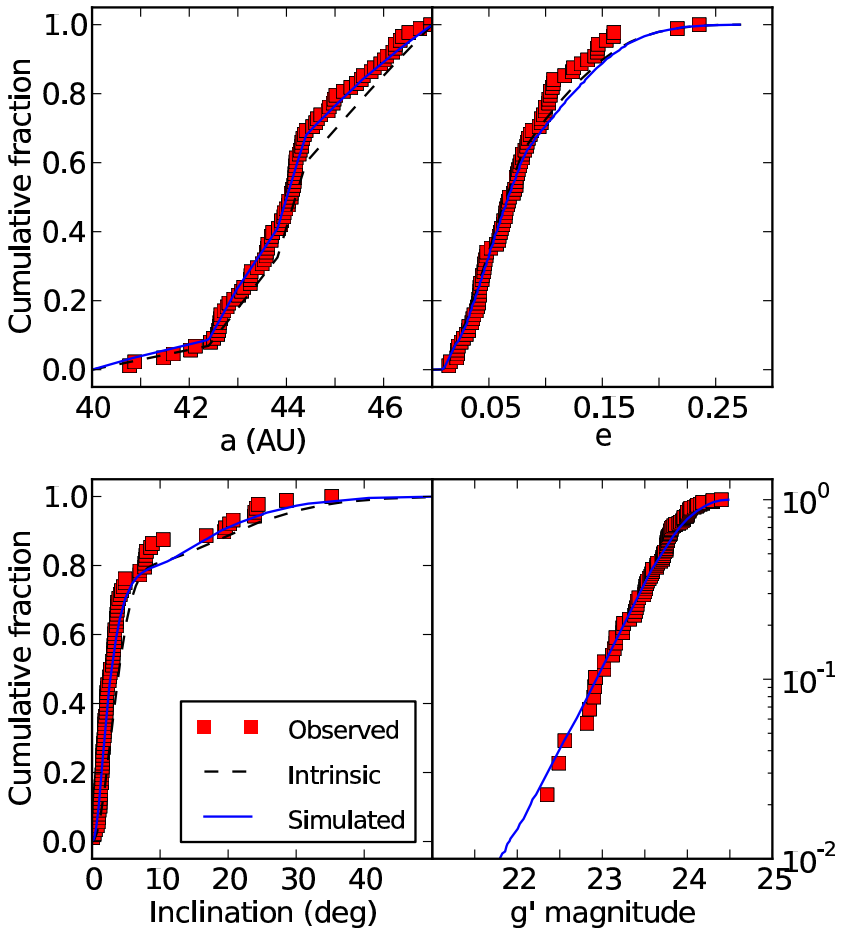

Fig. 6.— CFEPS+Pre objects (red solid squares) compared to our main-belt model's distribution in a (upper left), e (upper right), i (lower left) and g magnitude (lower right) distributions when the intrinsic (dashed line) are observed through the CFEPS Survey Simulator (resulting thin solid lines). The model used here is the one described in Section 5.1, with values of the parameters corresponding to our nominal case (see Section 5.1.2).

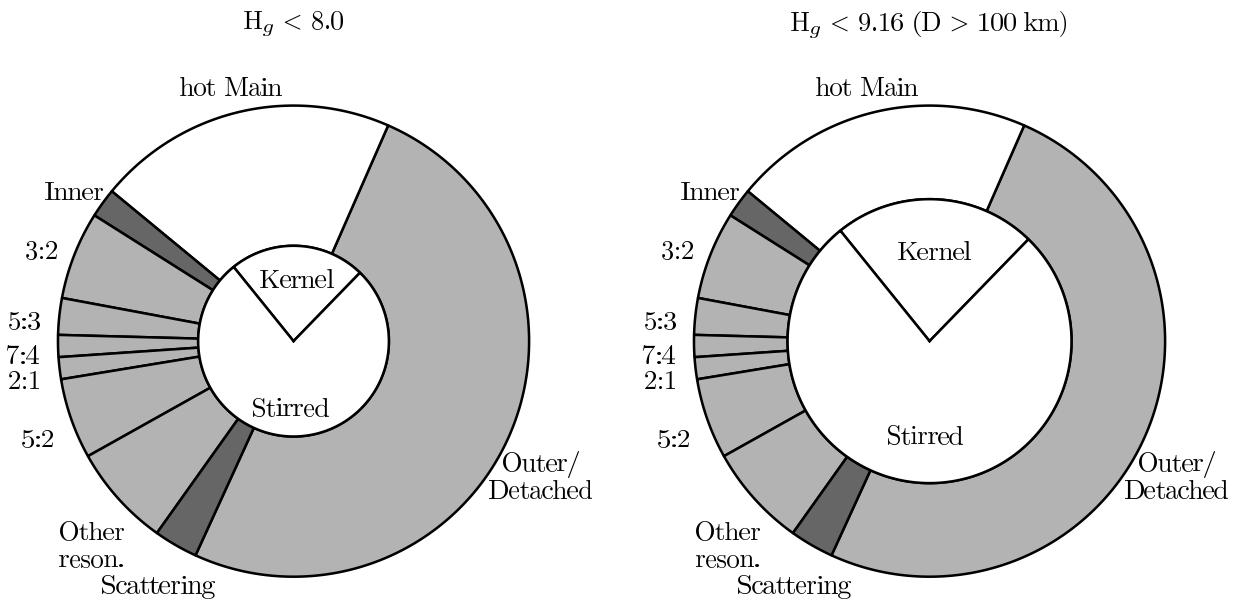

Fig. 7.— A representation of the fractional populations of the various dynamical classes measured in the L7 model. The surface area of each population shown is proportional to the relative population for objects with $H_g \leq 8$ (left) and $H_g \leq 9.16$ (right), corresponding to $D \geq 100$ km, assuming an albedo $p = 0.05$. The wedge label "Other reson." refers to resonant populations measured other than those individually labelled (4:3, 7:3, 5:4, 3:1, 5:1; see Gladman et al. 2011) . The outer annulus is comprised entirely of "hot" population objects while the "cold" populations, of which there is only the Kernel and Stirred components, are represented by the inner circle. The white area corresponds to the main belt.

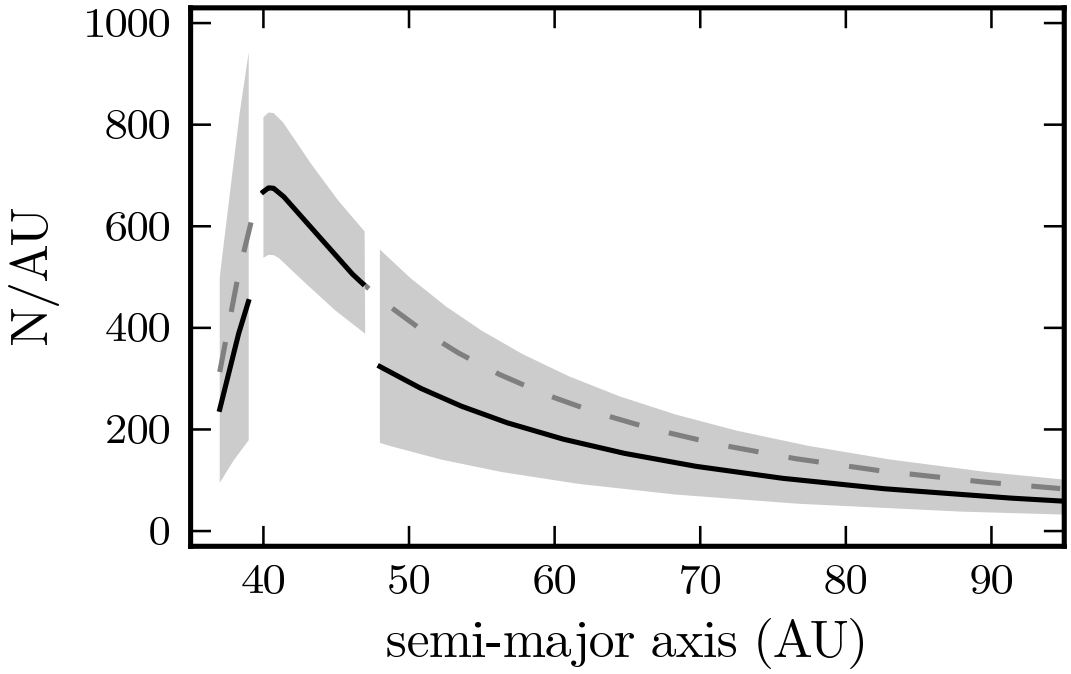

Fig. 8.— The linear number density (/AU) for three Kuiper Belt components: the inner belt ($a < 39$ AU), the hot main belt ($40 < a < 47$) and the outer plus detached belts ($a > 48$ AU). Each region's total population is scaled to the number with $H_g \leq 8$, as determined by our model population estimates. The inner belt's population has been scaled up by a factor of 1.85 to account for the ν_8 resonance (see footnote 5). The solid lines represent the model population determined *independently* for each zone while the grey dashed line indicates the smooth extension of the hot main belt model to the semi-major axis range occupied by the inner belt and the outer+detached populations, where the inner-belt decay at lower a occurs because of the rapidly-shrinking stable (a, q) phase-space volume available. A continuous primordial $a^{-2.5}$ hot population could, within uncertaties, account for all three populations. This suggests that these three Kuiper Belt components are a single dynamical population.

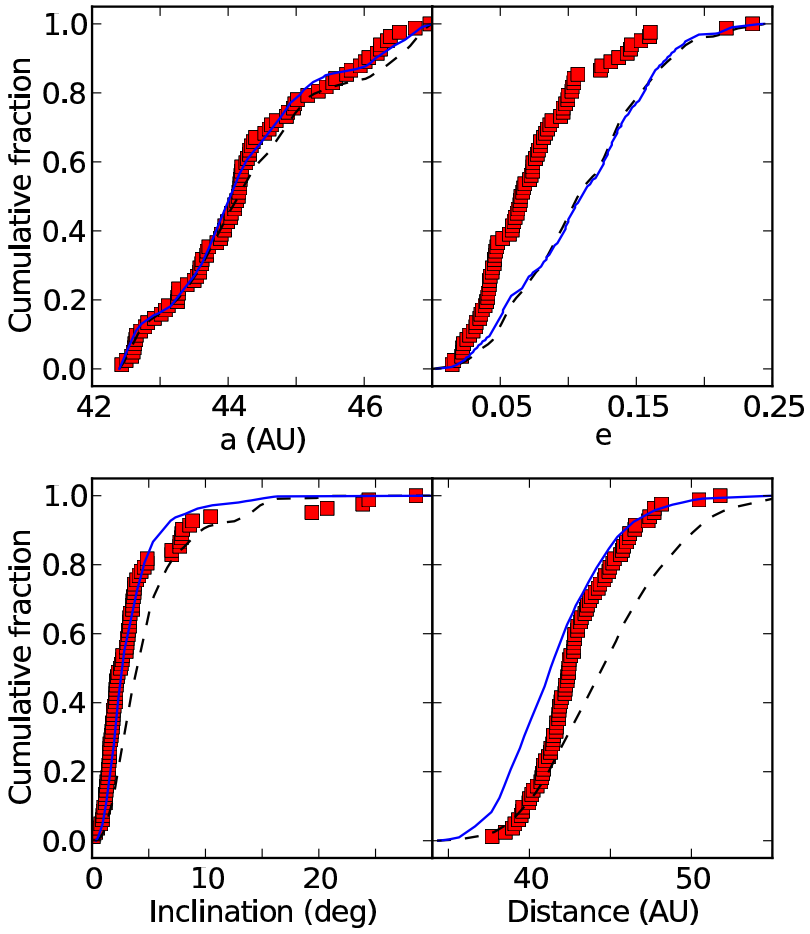

Fig. 9.— CFEPS+Pre objects (red solid squares) compared to the Nice model's distribution in a (upper left), e (upper right), i (lower left) and r (lower right) distributions when the intrinsic (black dashed line) distribution is biased via the CFEPS Survey Simulator (resulting blue solid lines). This shown case corresponds to a single-slope $\alpha = 1.1$ H_g distribution.

Table 7—Continued

Object	g	σ_g	N_g	r	σ_r	N_r	i	σ_i	N_i
L3y14PD	23.68	0.19	4	22.73	0.10	3	···	···	..
l3f05	23.71	0.18	3	···	···	..	···	···	..
l3h10	···	···	..	23.03	0.28	7	···	···	..
l3h15	···	···	..	23.74	0.27	7	···	···	..
l3h16	···	···	..	23.53	0.64	7	···	···	..
l3q05	23.68	0.16	4	···	···	..	···	···	..
l3q07	24.19	0.21	7	···	···	..	···	···	..
l3w14	23.98	0.20	3	···	···	..	···	···	..
l3w19	24.00	0.11	3	···	···	..	···	···	..
U3f02	24.07	0.21	4	23.41	0.31	3	···	···	..
U3h06	···	···	..	23.96	0.35	7	···	···	..
U3s04	24.10	0.45	6	···	···	..	···	···	..
U3w13	24.39	0.21	4	23.96	0.21	3	···	···	..
U3w16	24.07	0.14	4	···	···	..	23.14	0.25	3
U3w17	24.45	0.09	4	···	···	..	23.27	0.15	3
U3y04	24.25	0.13	4	22.57	2.16	4	···	···	..
U3y08	24.25	0.13	4	23.43	0.25	3	···	···	..
U3y16	23.93	0.37	4	23.45	0.16	3	···	···	..
u3h02	···	···	..	23.96	0.25	4	···	···	..
u3h03	···	···	..	24.01	0.09	3	···	···	..
u3h07	···	···	..	24.35	0.43	4	···	···	..
u3h12	···	···	..	23.79	0.23	7	···	···	..
u3h17	···	···	..	24.17	0.33	4	···	···	..
u3w12	24.43	0.15	3	···	···	..	23.48	0.26	3
u3w15	24.07	0.21	3	···	···	..	···	···	..
u3w18	24.49	0.19	3	···	···	..	···	···	..
u3y10	24.00	0.09	3	···	···	..	···	···	..
u3y13	24.28	0.16	3	···	···	..	···	···	..
L4h01PD	23.77	0.40	3	···	···	..	···	···	..
L4h02PD	23.50	0.18	3	···	···	..	···	···	..
L4h05PD	23.96	0.16	3	23.48	0.31	4	···	···	..
L4h06	23.83	0.12	3	22.77	0.75	2	···	···	..
L4h07	23.70	0.08	3	23.35	0.37	6	···	···	..
L4h08	23.01	0.03	4	22.72	0.13	3	22.41	0.14	3
L4h09PD	21.34	0.18	4	···	···	..	···	···	..
L4h10PD	22.96	0.09	4	···	···	..	22.62	0.16	3
L4h11	22.98	0.09	4	22.52	0.10	4	22.08	0.09	3
L4h12	24.11	0.34	4	22.92	0.35	4	22.60	0.01	3
L4h13	23.64	0.23	3	23.34	0.13	3	22.53	0.15	2
L4h14	23.68	0.30	4	23.65	0.31	3	···	···	..
L4h15	24.05	0.05	3	23.74	0.63	7	···	···	..
L4h16	24.04	0.45	3	23.38	0.25	3	···	···	..
L4h18	23.34	0.38	4	23.54	1.00	3	22.01	0.25	3
L4h21	23.75	0.05	3	23.43	0.32	3	23.00	0.12	3
L4j01	23.81	0.18	5	23.46	0.40	7	···	···	..
L4j02	23.35	0.09	5	22.59	0.13	7	22.37	0.12	3

Table 7—Continued

Object	g	σ_g	N_g	r	σ_r	N_r	i	σ_i	N_i
L4j03	23.87	0.13	5	23.06	0.18	7	22.91	0.15	3
L4j05	23.55	0.10	6	22.66	0.12	6	22.46	0.14	3
L4j06PD	22.13	0.04	4	21.70	0.03	4	21.74	0.04	2
L4j07	22.96	0.19	5	22.10	0.09	3	21.91	0.04	2
L4j08	23.51	0.16	5	22.79	0.20	7	22.43	0.32	3
L4j10	23.75	0.21	3	23.06	0.12	2	22.82	0.06	3
L4j11	23.55	0.32	8	23.04	0.30	5	22.77	0.26	3
L4j12	23.61	0.08	4	23.14	0.11	3	···	···	..
L4k01	24.01	0.12	3	23.11	0.17	2	23.03	0.11	3
L4k02	23.14	0.20	4	22.59	0.04	2	22.18	0.15	2
L4k03	23.54	0.28	4	22.97	0.34	9	22.25	0.05	3
L4k04	24.16	0.15	4	23.22	0.03	3	22.96	0.12	3
L4k09	23.69	0.22	4	22.53	0.29	3	22.34	0.19	4
L4k10	24.43	0.23	4	23.44	0.28	4	23.19	0.15	3
L4k11	23.32	0.15	4	22.99	0.10	3	22.58	0.07	2
L4k12	23.20	0.20	4	22.72	0.11	4	···	···	..
L4k13	23.99	0.16	3	23.15	0.12	3	23.03	0.17	3
L4k14	24.08	0.14	4	23.32	0.19	4	22.93	0.95	3
L4k15PD	23.22	0.07	4	22.48	0.17	3	22.12	0.02	2
L4k16	23.99	0.15	4	22.93	1.27	5	23.32	0.12	2
L4k17	23.07	0.17	4	22.55	0.12	5	22.33	0.05	3
L4k18	23.61	0.09	4	23.08	0.34	3	···	···	..
L4k19	23.66	0.29	4	23.40	0.17	6	···	···	..
L4k20	23.80	0.27	4	23.19	0.29	3	22.47	0.46	2
L4m01	23.83	0.14	5	···	···	..	···	···	..
L4m02	23.43	0.25	8	22.72	0.10	3	···	···	..
L4m03	23.57	0.39	5	23.33	0.21	3	···	···	..
L4m04	23.58	0.53	5	···	···	..	22.14	0.00	1
L4n03	23.72	0.11	4	···	···	..	22.72	0.49	3
L4n04	23.60	0.17	4	22.45	0.11	4	22.50	0.00	1
L4n05	23.69	0.24	4	···	···	..	23.05	0.15	2
L4n06	23.65	0.09	4	···	···	..	23.49	0.79	3
L4o01	22.98	0.09	4	22.21	0.39	3	21.95	0.76	3
L4p01	23.90	0.13	3	23.48	0.41	3	···	···	..
L4p02	23.83	0.20	4	23.07	0.14	2	···	···	..
L4p03	23.17	0.11	4	22.45	0.14	4	22.09	0.11	2
L4p04PD	21.96	0.14	4	22.33	1.43	4	21.58	0.09	3
L4p05	23.57	0.08	4	22.74	0.08	6	22.38	0.16	3
L4p06PD	22.34	0.10	4	21.81	0.23	4	21.56	0.30	3
L4p07	22.32	0.34	4	···	···	..	24.08	0.37	3
L4p08PD	23.81	0.21	4	···	···	..	22.87	0.14	3
L4p09	23.61	0.21	4	22.88	0.17	7	22.62	0.14	2
L4q03	23.57	0.07	3	23.01	0.09	7	···	···	..
L4q05	23.56	0.11	4	23.04	0.10	3	22.84	0.41	3
L4q06	23.97	0.24	4	23.54	0.19	3	23.83	0.43	3
L4q09	24.11	0.12	4	23.11	0.01	3	22.72	0.23	3

Table 7—Continued

Object	g	σ_g	N_g	r	σ_r	N_r	i	σ_i	N_i
L4q10	23.54	0.27	4	···	···	..	22.44	0.03	3
L4q11	23.92	0.14	4	···	···	..	22.81	0.16	3
L4q12PD	24.11	0.09	3	···	···	..	···	···	..
L4q14	23.59	0.15	7	···	···	..	22.89	0.34	3
L4q15	24.04	0.24	4	···	···	..	···	···	..
L4q16	23.71	0.17	4	···	···	..	20.17	0.00	1
L4v01	24.18	0.19	4	24.00	1.07	2	···	···	..
L4v02	23.80	0.02	4	23.01	0.27	3	···	···	..
L4v03	22.83	0.12	4	21.95	0.09	3	···	···	..
L4v04	24.13	0.09	4	23.32	0.22	3	23.45	0.23	2
L4v05	24.11	0.17	4	23.32	0.12	2	23.04	0.07	2
L4v06	23.66	0.15	4	23.03	0.11	3	22.51	0.12	2
L4v08	23.95	0.16	4	23.17	0.27	2	23.16	0.02	2
L4v09	23.52	0.08	5	23.03	0.08	4	22.83	0.09	3
L4v10	23.87	0.21	4	22.93	0.20	3	22.85	0.05	3
L4v11	24.16	0.20	4	23.64	0.77	4	23.58	0.17	3
L4v12	24.00	0.08	4	23.44	0.20	3	23.60	0.13	4
L4v13	22.72	0.09	4	22.68	0.70	5	22.32	0.02	3
L4v14	23.25	0.16	4	22.57	0.17	5	···	···	..
L4v18	22.95	0.22	3	22.66	0.15	4	22.57	0.27	2
l4h03	23.46	0.17	4	···	···	..	···	···	..
l4h04	23.89	0.17	3	···	···	..	23.48	0.21	3
l4h17	23.59	0.09	4	···	···	..	···	···	..
l4h19	23.91	0.39	4	···	···	..	···	···	..
l4k05	23.74	0.23	4	···	···	..	23.20	0.14	4
l4k06	24.16	0.23	4	···	···	..	23.96	0.32	2
l4k08	23.94	0.70	4	···	···	..	···	···	..
l4o02	23.79	0.37	5	23.53	0.38	3	···	···	..
l4q01	23.81	0.06	3	···	···	..	···	···	..
l4q02	23.77	0.20	4	···	···	..	···	···	..
l4q04	23.72	0.08	5	···	···	..	···	···	..
l4q08	23.30	0.11	3	···	···	..	···	···	..
l4v07	23.39	0.47	4	···	···	..	···	···	..
l4v16	24.30	0.43	3	···	···	..	···	···	..
l4v17	24.19	0.20	3	···	···	..	···	···	..
l4v19	23.99	0.43	3	···	···	..	···	···	..
U4j04PD	24.10	0.21	5	23.25	0.25	4	22.98	0.12	3
U4j09	24.19	0.30	2	23.29	0.17	6	22.83	0.23	3
U4n01	24.20	0.25	4	···	···	..	22.80	0.00	1
U4n02	24.13	0.32	4	···	···	..	21.50	1.11	3
u4h20	24.14	0.20	3	···	···	..	23.13	0.13	3
u4k07	24.61	0.25	3	···	···	..	···	···	..
u4q13	24.31	0.11	3	···	···	..	22.85	0.19	3
L5c02	23.59	0.13	2	22.65	0.07	4	22.42	0.06	3
L5c03	23.96	0.27	3	23.27	0.05	3	23.01	0.15	3
L5c06	24.27	0.22	5	···	···	..	22.68	0.73	3

Table 7—Continued

Object	g	σ_g	N_g	r	σ_r	N_r	i	σ_i	N_i
L5c07PD	22.94	0.11	5	22.17	0.12	2	22.01	0.08	3
L5c08	23.59	0.24	6	22.66	0.20	4	22.67	0.07	3
L5c10PD	24.02	0.05	3	···	···	..	23.10	0.11	3
L5c11	23.66	0.47	4	23.16	0.14	3	23.10	0.18	3
L5c12	22.28	0.04	4	···	···	..	21.19	0.02	3
L5c13PD	23.80	0.22	4	···	···	..	23.16	0.12	2
L5c14	23.41	0.09	3	···	···	..	22.61	0.07	3
L5c15	24.16	0.16	4	23.27	0.57	4	23.27	0.15	3
L5c16	23.08	0.16	4	22.67	0.05	3	22.63	0.11	2
L5c18	23.84	0.14	3	···	···	..	···	···	..
L5c19PD	23.76	0.55	3	23.24	0.28	4	23.17	0.08	3
L5c20PD	24.04	0.20	4	23.69	0.59	4	22.52	0.97	3
L5c21PD	23.75	0.20	3	22.84	0.10	4	22.79	0.14	3
L5c22	23.59	0.19	4	22.83	0.07	3	22.48	0.03	3
L5c23	24.19	0.09	3	23.37	0.07	4	23.27	0.16	4
L5c24PD	23.84	0.40	3	···	···	..	22.86	0.90	4
L5i01	23.66	0.27	4	···	···	..	···	···	..
L5i02PD	23.85	0.16	4	···	···	..	···	···	..
L5i03PD	23.77	0.21	4	22.97	0.58	3	···	···	..
L5i04	23.07	0.21	7	···	···	..	···	···	..
L5i05	23.81	0.21	4	···	···	..	···	···	..
L5i06PD	23.12	0.05	4	···	···	..	22.41	0.20	3
L5i08	23.20	0.61	4	···	···	..	22.41	0.08	3
L5j02	23.29	0.11	5	22.20	0.18	3	···	···	..
L5j03	23.16	0.07	3	22.50	0.10	3	22.23	0.05	4
L5j04	22.51	0.11	5	21.64	0.18	3	21.52	0.15	2
L5r01	23.65	0.22	4	···	···	..	···	···	..
L5s01PD	20.84	0.02	3	···	···	..	···	···	..
l5c01	24.05	0.55	5	···	···	..	···	···	..
l5c04	24.21	0.33	6	···	···	..	···	···	..
U5c17PD	24.18	0.30	3	···	···	..	23.46	0.14	3
U5j01PD	23.83	0.16	5	23.37	0.24	3	···	···	..
U5j06	23.67	0.23	5	23.11	0.25	4	23.06	0.16	3
u5c09	24.35	0.21	2	···	···	..	···	···	..
u5i07	24.29	0.41	4	···	···	..	22.92	0.21	3
u5j05	23.50	0.06	5	···	···	..	22.83	0.09	2
L7a02	23.50	0.33	3	···	···	..	22.74	0.13	4
L7a03	23.80	0.07	4	23.26	0.12	4	23.27	0.15	3
L7a04PD	23.29	0.11	4	···	···	..	21.92	0.09	3
L7a05	23.68	0.20	4	22.85	0.00	1	22.82	0.38	3
L7a06	23.78	0.13	4	···	···	..	22.92	0.12	4
L7a07	23.43	0.20	4	22.75	0.11	3	22.55	0.11	4
L7a10	23.63	0.04	4	23.35	0.22	4	23.26	0.11	3
L7a11PD	23.34	0.16	5	22.64	0.10	4	22.67	0.10	4
l7a12	23.86	0.13	6	···	···	..	···	···	..
U7a01	24.13	0.16	4	23.29	0.26	4	22.94	0.27	2

C. Appendix C

Comparing previously-published population estimates of the main classical belt, either as a whole or for the various components, with our present values must ensure that the same limiting H_g magnitude and the same region of the phase space are adopted. The main difference between P1 and the present L7 model is the higher q cut-off that was applied to the P1 sample. Restricting our current sample to the same region of phase space as was modeled in P1 gives very similar population estimates for the main belt. Secondly, P1's cold component was restricted in extend to $a \leq 45$ AU and hence had a smaller population than in our current model, and conversely, the hot population was slightly overestimated compared to our current value, for the region of phase space. Lastly, because we use widely different H-magnitude slopes, the population estimates should be compatible for the detected H_g=7–8 range, but diverge for smaller TNOs (larger H). Scaling P1 to the H_g=8 limit, we find

$$N_{\rm P1}({\rm H}_g \leq 8.0) = 4400^{+1800}_{-1100},$$

while restricting our currennt model to the same phase space gives

$$N_{\rm All}({\rm H}_g \leq 8.0) = 5800^{+1300}_{-1200},$$

in reasonable agreement.

The latest independant population estimate of the main classical belt was done by Trujillo et al. (2001), who estimate $38{,}000^{+5400}_{-2700}$ objects bigger than $D = 100$ km, with uncertainties being 3σ confidence. This number is more than 3 times smaller than our H_g=9.16 estimate. Can the two numbers be reconciled ?

First, one must match the size ranges of the population being estimated. Trujillo et al. used a red albedo p_R=0.04 and a solar red magnitude of -27.1. In this case a TNO of $D = 100$ km has an absolute magnitude ${\rm H}_R = 8.8$. Assuming the same g - R=0.8 color as we used in Kavelaars et al. (2009), this corresponds to ${\rm H}_g = 9.6$. When looking at Fig. 9 of Trujillo et al. (2001) one clearly sees that either the assumption of an exponential luminosity function breaks at around $m_R \sim 24$, or the debiasing is incorrect faintward of that value. In particular, the lack of debiased objects fainter than 24 would push the population estimate down. For the main belt model used by Trujillo et al., $m_R = 24$ corresponds to ${\rm H}_R \sim 7.7$ or ${\rm H}_g \sim 8.5$. Hence their population estimate is probably more applicable to that limit but not to smaller sizes. With $q = 4$, or $\alpha = 0.6$, the population estimates of Trujillo et al. (2001) is

$$N_{\rm Trujillo}({\rm H}_g \leq 8.5) = 8300^{+1200}_{-600}.[3\sigma]$$

Restricting our model to the same phase space and extrapolating our population estimate out to ${\rm H}_g \leq 8.5$, we obtain

$$N_{\rm All}({\rm H}_g \leq 8.5) = 19,000^{+4100}_{-3700}, [95\% confidence]$$

a factor of 2 larger than Trujillo et al. (2001) However, this last number is an extrapolation beyond the limit to which CFEPS really measured the population. A more secure comparison from our point of view is done for ${\rm H}_g \leq 8.0$. The numbers become

$$N_{\rm Trujillo}({\rm H}_g \leq 8.0) = 4200^{+600}_{-300},$$

and

$$N_{\rm All}({\rm H}_g \leq 8.0) = 5500^{+1300}_{-1100}.[95\% confidence]$$

Hence we marginally agree with Trujillo et al. (2001) at $\rm H_g \leq 8.0$. At $\rm H_g > 8.0$, an extrapolation of our result (using our two H slopes determined at larger sizes) rapidly diverges from the Trujillo et al. (2001) estimate; if the slope does indeed drop near H $\sim$8 (or R $\simeq$24) to a shallower slope (Fuentes & Holman 2008) then the two estimates are less discrepant.

Acknowledgements

This research was supported by funding from the Natural Sciences and Engineering Research Council of Canada, the Canadian Foundation for Innovation, the National Research Council of Canada, and NASA Planetary Astronomy Program NNG04GI29G. This project could not have been a success without the dedicated staff of the Canada-France-Hawaii telescope as well as the assistance of the skilled telescope operators at KPNO and Mount Palomar.

We dedicate this paper to the memory of Brian G. Marsden, for his devotion to orbital determination and passionate encouragement to observational planetary astronomers.

Facilities: In addition to CFHT (MegaPrime) this work was made possible thanks to access to facilities listed in Table 2.

REFERENCES

Allen, R. L., Bernstein, G. M., & Malhotra, R. 2001, ApJ, 549, L241

—. 2002, AJ, 124, 2949

Allen, R. L., Gladman, B., Kavelaars, J. J., Petit, J.-M., Parker, J. W., & Nicholson, P. 2006, ApJ, 640, L83

Bernstein, G. M., Trilling, D. E., Allen, R. L., Brown, M. E., Holman, M., & Malhotra, R. 2004, AJ, 128, 1364

Bowell, E., Hapke, B., Domingue, D., Lumme, K., Peltoniemi, J., & Harris, A. W. 1989, in Asteroids II, ed. R. P. Binzel, T. Gehrels, & M. S. Matthews, 524–556

Brown, M. E. 2001, AJ, 121, 2804

—. 2008, in The Solar System Beyond Neptune, ed. Barucci, M. A., Boehnhardt, H., Cruikshank, D. P., & Morbidelli, A. , LPI (Tuscon: University of Arizona Press), 335–344

Brown, M. E., Barkume, K. M., Ragozzine, D., & Schaller, E. L. 2007, Nature, 446, 294

Brown, M. E., & Pan, M. 2004, AJ, 127, 2418

Chiang, E. I. 2002, ApJ, 573, L65

Chiang, E. I., Lovering, J. R., Millis, R. L., Buie, M. W., Wasserman, L. H., & Meech, K. J. 2003a, Earth Moon and Planets, 92, 49

Chiang, E. I., et al. 2003b, AJ, 126, 430

Duncan, M. J., & Levison, H. F. 1997, Science, 276, 1670

Duncan, M. J., Levison, H. F., & Budd, S. M. 1995, AJ, 110, 3073

Elliot, J. L., et al. 2005, AJ, 129, 1117

Fraser, W. C., Brown, M. E., & Schwamb, M. E. 2010, Icarus, 210, 944

Fraser, W. C., & Kavelaars, J. J. 2009, AJ, 137, 72

Fuentes, C. I., George, M. R., & Holman, M. J. 2009, ApJ, 696, 91

Fuentes, C. I., & Holman, M. J. 2008, AJ, 136, 83

Fukugita, M., Ichikawa, T., Gunn, J. E., Doi, M., Shimasaku, K., & Schneider, D. P. 1996, AJ, 111, 1748

Gladman, B., & Chan, C. 2006, ApJ, 643, L135

Gladman, B., Holman, M., Grav, T., Kavelaars, J., Nicholson, P., Aksnes, K., & Petit, J.-M. 2002, Icarus, 157, 269

Gladman, B., Kavelaars, J. J., Petit, J.-M., Morbidelli, A., Holman, M. J., & Loredo, T. 2001, AJ, 122, 1051

Gladman, B., et al. 2006, Minor Planet Electronic Circulars, 2006-H29

—. 2009, ApJ, 697, L91

—. 2011, AJ, submitted, 1, 1

Gladman, B. J., Marsden, B. G., & van Laerhoven, C. 2008, in The Solar System Beyond Neptune, ed. A. Barucci, H. Boehnhardt, D. Cruikshank, & A. Morbidelli, LPI (Tucson: University of Arizona Press), 43–57

Gomes, R. S. 2003, Icarus, 161, 404

Gomes, R. S., Morbidelli, A., & Levison, H. F. 2004, Icarus, 170, 492

Gulbis, A. A. S., Elliot, J. L., Adams, E. R., Benecchi, S. D., Buie, M. W., Trilling, D. E., & Wasserman, L. H. 2010, AJ, 140, 350

Gulbis, A. A. S., Elliot, J. L., & Kane, J. F. 2006, Icarus, 183, 168

Hahn, J. M., & Malhotra, R. 2005, AJ, 130, 2392

Hainaut, O. R., & Delsanti, A. C. 2002, A&A, 389, 641

Ida, S., Larwood, J., & Burkert, A. 2000, ApJ, 528, 351

Information Technology Laboratory, N. 2011, NIST/SEMATECH e-Handbook of Statistical Methods, Tech. rep., National Institute of Standards and Technology, U.S. Commerce Department

Ivezic, Z., et al. 2008, Serbian Astronomical Journal, 176, 1

Jewitt, D., Luu, J., & Chen, J. 1996, AJ, 112, 1225

Jewitt, D., Luu, J., & Trujillo, C. 1998, AJ, 115, 2125

Jewitt, D. C., & Luu, J. X. 1995, AJ, 109, 1867

Johnstone, D., Hollenbach, D., & Bally, J. 1998, ApJ, 499, 758

Jones, R. L., Parker, J. W., Bieryla, A., Marsden, B. G., Gladman, B., Kavelaars, J., & Petit, J. 2010, AJ, 139, 2249

Jones, R. L., et al. 2006, Icarus, 185, 508

Kavelaars, J., Allen, L., Gladman, B., Petit, J.-M., van Laerhoven, C., Nicholson, P., Margot, J.-L., & Marsden, B. G. 2006a, Minor Planet Electronic Circulars, 2006-H35

—. 2011, Minor Planet Electronic Circulars, 2011-

947 Kavelaars, J., Jones, L., Gladman, B., Parker, J. W., & Petit, J.-M. 2008, in The Solar System Beyond
948 Neptune, ed. M. A. Barucci, H. Boehnhardt, D. P. Cruikshank, & A. Morbidelli (Tucson: University
949 of Arizona Press), 59–69

950 Kavelaars, J., et al. 2006b, Minor Planet Electronic Circulars, 2006-H30

951 Kavelaars, J. J., et al. 2009, AJ, 137, 4917

952 Larsen, J. A., et al. 2001, AJ, 121, 562

953 Leinhardt, Z. M., Marcus, R. A., & Stewart, S. T. 2010, ApJ, 714, 1789

954 Levison, H. F., Morbidelli, A., Vanlaerhoven, C., Gomes, R., & Tsiganis, K. 2008, Icarus, 196, 258

955 Lykawka, P. S., & Mukai, T. 2007, Icarus, 189, 213

956 Magnier, E. A., & Cuillandre, J.-C. 2004, PASP, 116, 449

957 Malhotra, R. 1993, Nature, 365, 819

958 Mann, R. K., & Williams, J. P. 2009, ApJ, 694, L36

959 —. 2010, ApJ, 725, 430

960 Millis, R. L., Buie, M. W., Wasserman, L. H., Elliot, J. L., Kern, S. D., & Wagner, R. M. 2002, AJ, 123,
961 2083

962 Morbidelli, A., Bottke, W., Nesvorný, D., & Levison, H. 2009a, Icarus, 204, 558

963 Morbidelli, A., Brasser, R., Tsiganis, K., Gomes, R., & Levison, H. F. 2009b, A&A, 507, 1041

964 Morbidelli, A., Emel'yanenko, V. V., & Levison, H. F. 2004, MNRAS, 355, 935

965 Morbidelli, A., & Levison, H. F. 2004, AJ, 128, 2564

966 Morbidelli, A., Levison, H. F., Tsiganis, K., & Gomes, R. 2005, Nature, 435, 462

967 Nagasawa, M., & Ida, S. 2000, AJ, 120, 3311

968 Parker, A. H., & Kavelaars, J. J. 2010, ApJ, 722, L204

969 Petit, J.-M., Holman, M., Scholl, H., Kavelaars, J., & Gladman, B. 2004, MNRAS, 347, 471

970 Petit, J.-M., Holman, M. J., Gladman, B. J., Kavelaars, J. J., Scholl, H., & Loredo, T. J. 2006, MNRAS, 365,
971 429

972 Petit, J.-M., Kavelaars, J. J., Gladman, B., & Loredo, T. 2008, in The Solar System Beyond Neptune, ed.
973 M. A. Barucci, H. Boehnhardt, D. P. Cruikshank, & A. Morbidelli (Tucson: University of Arizona
974 Press), 71–87

975 Romanishin, W., Tegler, S. C., & Consolmagno, G. J. 2010, AJ, 140, 29

976 Schwamb, M. E., Brown, M. E., Rabinowitz, D. L., & Ragozzine, D. 2010, ApJ, 720, 1691

977 Stark, C. C., & Kuchner, M. J. 2010, in Bulletin of the American Astronomical Society, Vol. 42, Bulletin of
978 the American Astronomical Society, 527–+

979 Stepinski, T. F., & Valageas, P. 1996, A&A, 309, 301

980 —. 1997, A&A, 319, 1007

981 Thommes, E. W., Duncan, M. J., & Levison, H. F. 1999, Nature, 402, 635

982 Throop, H. B., & Bally, J. 2005, ApJ, 623, L149

983 Trujillo, C. A., & Brown, M. E. 2001, ApJ, 554, L95

984 —. 2003, Earth Moon and Planets, 92, 99

985 Trujillo, C. A., Jewitt, D. C., & Luu, J. X. 2000, ApJ, 529, L103

986 —. 2001, AJ, 122, 457

987 Tsiganis, K., Gomes, R., Morbidelli, A., & Levison, H. F. 2005, Nature, 435, 459

988 Youdin, A. N. 2011, ArXiv e-prints

Table 7—Continued

Object	g	σ_g	N_g	r	σ_r	N_r	i	σ_i	N_i
U7a08	24.00	0.18	4	23.62	0.14	4	23.25	0.32	3
U7a09	24.11	0.21	3	23.45	0.16	4	23.41	0.28	3

Note. — 'L' objects are the tracked, characterized (i.e. with flux above the 40% detection efficiency level) objects of CFEPS. 'l' objects are the non-tracked, characterized objects of CFEPS. There is no ephemeris-based bias in those losses. Most of them were not recovered at checkup (either too faint or sheared out of field coverage westward). 'U' objects are the tracked, non-characterized (i.e. with flux below 40% detection efficiency level) objects of CFEPS. 'u' objects are the non-tracked, non-characterized objects of CFEPS. Magnitudes listed for photometric observations from CFHT. Some numbers are missing because the corresponding object was not re-observed in a particular filter from CFHT in photometric conditions. This is the case for lost objects, some of the PD objects which we did not try to track, or objects tracked solely at other facilities. g, r, i columns give the apparent magnitude of the object in the correspondant filter. σ_x is the uncertainty on the magnitude in filter x. N_x is the number of measurements in filter x used to derive the apparent magnitude and its uncertainty.